Evaluation of the Effects of Bolus Air Gaps on Surface Dose in Radiation Therapy and Possible Clinical Implications

by

Adam Shaw

M.Sc., University of Oxford, 2009

A THESIS SUBMITTED IN PARTIAL FULFILLMENT
OF THE REQUIREMENTS FOR THE DEGREE OF

Master of Science

in

THE FACULTY OF GRADUATE AND POSTDOCTORAL STUDIES
(Physics)

The University of British Columbia
(Vancouver)

August 2018

The following individuals certify that they have read, and recommend to the Faculty of Graduate and Postdoctoral Studies for acceptance, the thesis entitled:

Evaluation of the Effects of Bolus Air Gaps on Surface Dose in Radiation Therapy and Possible Clinical Implications

submitted by **Adam Shaw** in partial fulfillment of the requirements for the degree of **Master of Science** in **Physics**.

Examining Committee:

Cheryl Duzenli, Physics and Astronomy
Supervisor

Bradford Gill, BC Cancer Agency
Supervisory Committee Member

Abstract

In clinical radiotherapy, treatments are frequently delivered using photons with energies in the Megavoltage range. The advantage of such beam energies is that the majority of dose is deposited deeper within the patient, with the depth of maximum dose being up to several centimetres beyond the patient's skin. This effect allows radiotherapists to target tumours on organs such as the prostate. However, there are times when larger doses must be deposited to the near-skin region. In these cases, a layer of "substitute tissue" called a **bolus** is applied, to shift dose towards the patient's skin. Given the natural contours of the human body, it is difficult for a bolus to achieve perfect contact with the patient and air gaps are often present between the applied bolus and the patient's surface. Such air gaps have the potential to disturb the distribution of surface dose. In this thesis we present an investigation into the magnitude of the effects of bolus-surface air gaps on 6 MV photon beam surface dose.

Using a combination of ionization chamber measurements, film dosimetry, and Monte Carlo simulations, we establish that surface dose is significantly reduced in the presence of an air gap. The observed reduction in dose increases as the distance between the bolus material and the phantom surface increases, and is more severe at smaller field sizes.

By examining simulated and experimentally measured surface-dose-profiles, we demonstrate that bolus-surface gaps alter the shape of the dose distribution near the field boundary. We find that surface dose is reduced near the inside of the field edge, with a corresponding increase in dose in

the region outside of the defined field. We propose that this effect is caused by low-energy electrons that are generated within the bolus material, near the field edges, but are then scattered outside of the treatment region when passing through the air gap. As such we would recommend that care be taken to reduce the size of any air gaps to below 1 cm, especially in cases with weaker treatment beams and where the PTV is located near to at-risk organs.

Lay Summary

The use of X-rays to treat cancer requires precise control over the amount of radiation dose delivered by the treatment beam. Most clinical X-rays are in the Megavoltage energy range, which allows radiation to penetrate deeper into tissue and deliver the majority of dose up to several centimetres beyond the patient's skin. This allows the treatment of internal organs but is not suitable to address tumours closer to the skin. In such cases, radiotherapists may apply a layer of artificial tissue upon the body. The energy is allowed to build-up within this layer so the maximum the dose is delivered closer to the patient's skin. However, the presence of air gaps between the skin surface and this layer of "bolus" material can effect the distribution of dose. In this thesis, we present an investigation into the effects of such air gaps and discuss possible implications for radiotherapy treatments.

Preface

This dissertation is original and independent work by the author, Adam Shaw. None of the text of the dissertation is taken directly from previously published or collaborative articles.

Table of Contents

List of Tables

List of Figures

Abbreviations

IMRT Intensity Modulated Radiotherapy

TPS Treatment Planning System

PDD Percentage Depth Dose

MC Monte Carlo

AAA Analytical Anisotropic Algorithm

VMAT Volumetric Modulated Arc Therapy

BCCA BC Cancer Agency

MLC Multi-leaf collimator

QA Quality Assurance

PTV Planning Target Volume

CTV Clinical Target Volume

ECLIPSE^{TM} Eclipse Treatment Planning System - Developed by Varian Medical Systems

TLD Thermoluminescent Dosimeter

DRF Dose Reduction Factor

PP Parallel-plate

Acknowledgments

The work of study and research that has gone into producing this thesis would never have been completed without the support of many dear friends and colleagues.

First, I would like to thank my family of all they have done for me: Ashley, my dear wife, for her continual love and support, and James, my tiny man, for being a constant source of joy and inspiration. Also, thank you to my beagles, Bucky and Harley, for not eating my thesis.

Thank you to my supervisors, Cheryl Duzenli and Brad Gill, for the immense patience and helpful advice that has made this work possible. I would also like to thank all of my colleagues in the Department of Medical Physics and the BC Cancer Agency; especially Dr Tony Popescu and Parmveer Atwal, for helping to get me started with the Monte Carlo simulations, and Joel Beaudry for his assistance with the experiments.

Finally, I want to express how much I have valued the opportunity to work at the BC Cancer Agency. The importance of the work done by the BCCA cannot possibly be overstated and I am very proud to have contributed, if in a small way, to that great work.

Chapter 1

Introduction to Radiotherapy Physics

1.1 Introduction

In clinical radiotherapy, a primary role of the physicist is to ensure that a patient receives the correct quantity of radiation (i.e. dose) to the target volume, as prescribed by the radiation oncologist. To perform this task, physicists must understand the many factors that affect how radiation spreads through, and is absorbed by, living tissue. Many of the fundamental mechanisms underpinning these processes are well-understood. However, modern radiotherapy offers many options with regards to patient set-up, beam geometry and the modification of beam properties. The effect these various factors have on patient dose have to be carefully studied and quantified to ensure safe and accurate treatment planning and delivery.

In the work described in this thesis, we shall focus on challenges regarding the application of **bolus** in modern radiotherapy. Further discussion of the physics that necessitates the use of bolus in clinical situations shall follow later in this chapter. In brief, the term bolus is used to refer to any material that is placed on the patient's skin as a form of "artificial tissue". Current radiotherapy treatments primarily use beam energies in the **Megavoltage** (MV) range. At these energies the maximum dose is deposited deeper in the tissues, to allow treatment of internal structures such

as lungs and the prostate. However, it is often necessary to treat structures closer to the skin. By adding a layer of additional "tissue" through which the beam must penetrate, the region of maximum dose deposition is effectively shifted towards the surface. However, given the contours of the human body and possible interference from treatment apparatus (e.g. patient immobilizing masks) it is often not possible to place the bolus in full contact with the skin, leading to the presence of gaps between bolus and patient. The aim of this research project has been to elucidate the effect that these gaps have on the distribution of surface dose.

To set this question into its full context, it is first necessary to understand the effects that radiation has on tissue and how they may be meaningfully quantified and measured, i.e. it is necessary to understand what is meant by **dose**.

1.2 Interactions of Radiation in Matter

The term radiation refers to the propagation of energy through a medium via the action of some form of particles. These particles can be charged (e.g. protons), uncharged (neutrons), or even massless (photons). In this work we shall be concerned with the behaviour of X-rays, which are streams of high-energy photons, and are the most commonly used form of radiation in clinical practise.

As photons pass through matter they interact with the atoms through absorption or scattering processes, as listed below. It is impossible to predict which particular photon will undergo which interaction, rather, only the relative probabilities of these events can be discussed. The probability of each interaction is determined by its *attenuation coefficient* μ, which represents the probability that a photon will experience a specified interaction per until length travelled in the medium [26] [29]. As the probability of a photon interacting with the medium's atoms will depend on how closely they are packed (i.e. their density), a more useful quantity is the *mass attenuation coefficient*, which is simply the attenuation coefficient divided by the density μ/ρ.

Another key factor influencing the probability that an incident photon undergoes a given interaction, rather than some other process, is its energy. Scattering events can loosely be described as collisions between incident photons and the electrons of an atom. It is the energy of the photon, relative to the binding energy of the electron, that determines whether the photon is"strong" enough to transfer sufficient energy to knock out the electron (Compton scattering) or if the photon rebounds elastically, retaining all of its initial kinetic energy but travelling in a new direction (Rayleigh Scattering) [29]. In absorption events, the photon's energy has to be equal or higher than some threshold value, either the binding energy (photoelectric effect) or the rest mass of an electron-position pair (pair production) for the event to occur at all. Figure 1.1 shows the relationship between the mass attenuation coefficient and the incident energy for photons propagating in water.

Rayleigh Scattering In this process, the incident photon is deflected by the bound electrons that surround the nucleus. This primarily occurs when the energy of the incoming photon is very small compared to the binding energy of the atom's electrons, and simply "bounces off". As there is no transfer of energy from the photon to the medium, this interaction does not contribute to dose.

Compton Scattering When the energy of the incident photon is much higher than the binding energies of the atom's electrons, the electron can be approximately considered as unbound or "free". When the photon "collides" with the electron it transfers some of its energy and momentum and the electron is sent travelling through the medium. The photon also continues to propagate, albeit in a new direction, having lost some energy, and can undergo further interaction events.

Photoelectric Emission At energies comparable to the binding energy of the medium, the photon can be absorbed, transferring all of its energy to ionize an electron in the atom's core shells.

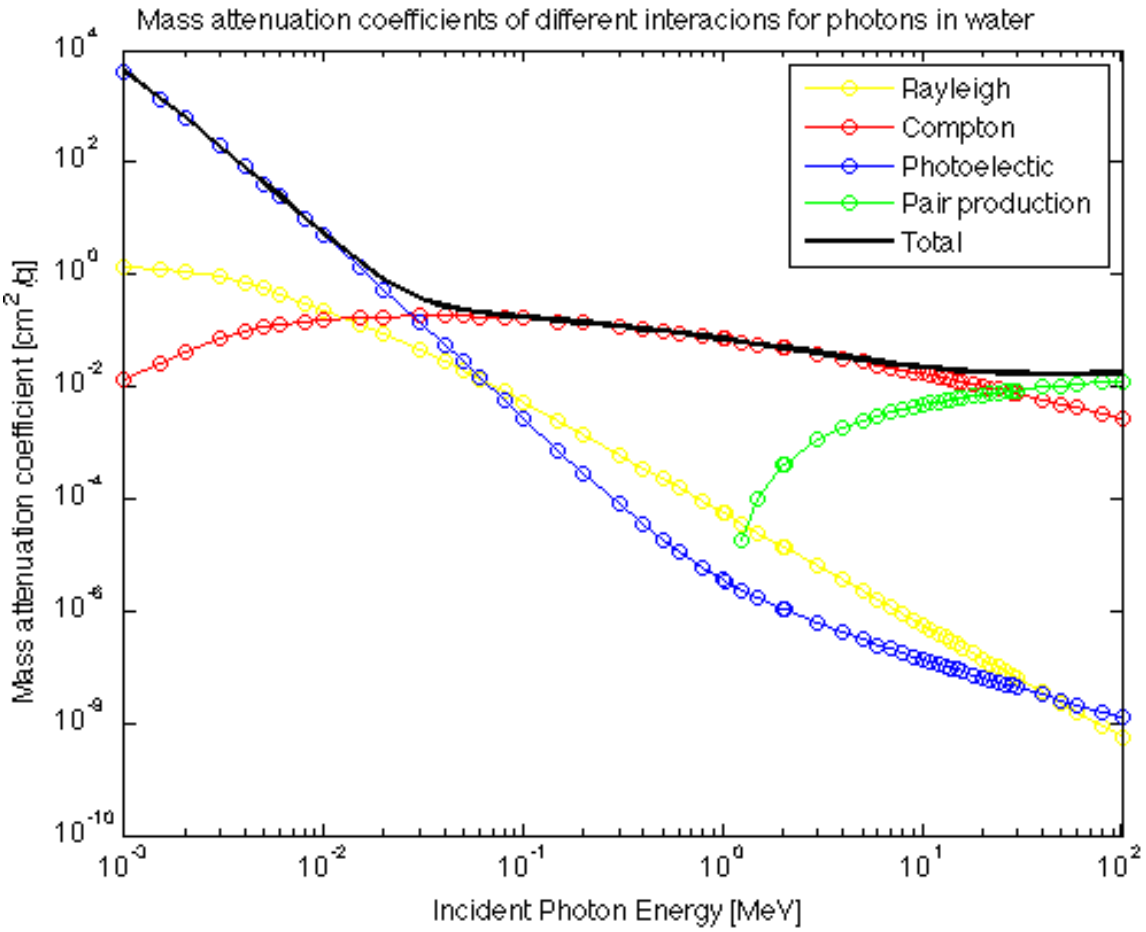

Figure 1.1: Plot showing the relationship between the probability of a photon undergoing one of the four specified interaction events in water, as quantified by the mass attenuation coefficient, and its energy. The solid black line represents the total mass attenuation coefficient μ/ρ, defined as the sum of the separate attenuation coefficients of each interaction. This figure was constructed using data freely available from NIST. [1]

Much of the original photon energy is used in unbinding the core electron, however, any additional energy is turned to kinetic energy so the newly free electron is emitted into the medium.

Pair/Triplet Production At high enough energies the photon can interact with the strong electric field surrounding the atomic nucleus, triggering the spontaneous decay of the photon into two

charged particles, an electron and a positron (an anti-electron). As with the photoelectric effect, this absorption process can only occur if the incident photon has energy above a certain threshold. In this case, that threshold is 1.022 MeV, which is the energy necessary to constitute the rest-mass of both electron and positron. Above this threshold, the additional photon energy is given to the newly formed particles as kinetic energy.

With the exception of Rayleigh scattering, in each of the four processes described above, transfer of energy from incident photons causes the release of energetic electrons into the medium. Unlike photons, electrons deposit energy into the medium through a continuous series of successive interactions with the electric fields that surround atoms. Some of these interactions can produce additional photons (*Bremsstrahlung*), however, most are simple collisional processes. The energy deposited by the electron, per unit distance, is quantified by the stopping power S. As with the attenuation coefficient for photons, this quantity is often normalized by the medium's density and this quantity is called the *mass stopping power*.

$$\frac{S}{\rho} = \frac{1}{\rho}\frac{dE}{dx} \tag{1.1}$$

The majority of the energy lost through electron collisions is dissipated as heat [29]. However, some fraction of this energy may trigger radiochemical changes in the medium, such as ionization of atoms and the formation of free radicals. In living tissue, such biochemical alteration of the DNA can potentially prohibit the reproduction of cells and lead to the death of the tissue. It is in this way, that radiation can be used to destroy cancer cells.

1.3 Dose, Kerma and Electronic Equilibrium

As described in the previous section, the deposition of energy to a medium from X-ray radiation is a process that occurs in two steps:

- Photons transfer kinetic energy to electrons via instantaneous Compton, Pair-production and Photoelectric interactions.

- These electrons deposit energy through successive collisional interactions as they travel through the medium. This energy is absorbed by the medium leading to the desired clinical effect.

To quantify the energies involved, separately, in each of these steps, two quantities are used: Kerma and Dose.[26]

Kerma, or Kinetic Energy Released in Medium, represents the energy *transferred* to electrons by photon interactions. **Dose** describes the energy that is actually *absorbed* by the medium. Both quantities are defined in dimensions of energy/mass, the standard unit of measurement in called the Gray: $1\,Gy = 1\,J/kg$.

One key distinction between these closely related concepts, is that the transfer of kerma is localized where the photon interaction occurred. Dose is deposited into the material more gradually as electrons pass through. The distribution of dose, therefore, is dependent on the fluence and range of the electrons released. As the photon beam enters the medium, interactions will occur that will trigger the release of electrons from that location. Those electrons will still be propagating through the medium even as the photons travel deeper and send out even more electrons. Newly liberated electrons join existing electrons as they stream through the material depositing dose, and so on, creating growing cascade of electrons and rapid build-up of dose. Figure 1.2 illustrates this process.

In Figure 1.2, photons (red arrows) penetrate the medium, undergoing interactions and triggering streams of electrons (blue arrows). For illustrative purposes, the majority of the electrons energies are deposited into the material at the end of their tracks, as shown by the green stars. In the near-surface region (boxes A and B), electrons are released but little energy is absorbed by the medium and so less dose is deposited into this region. Dose gradually builds up as photons pass

deeper into the medium. Starting from box C, at a depth exceeding the mean range of the electrons, the release of electrons becomes coincident with the deposition of the large amounts of dose. At this point, the transfer of kerma and the deposition of dose can be considered in equilibrium, a state referred to as *electronic equilibrium*.

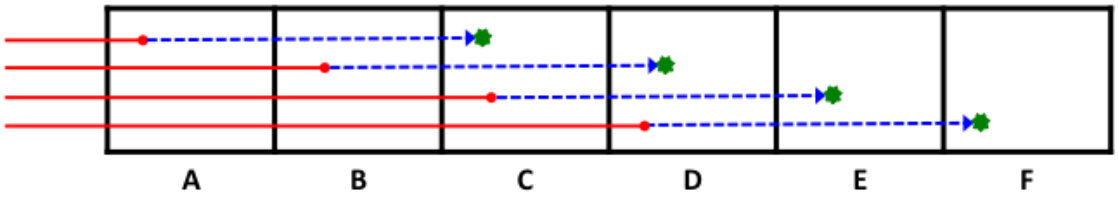

Figure 1.2: A schematic illustration showing the formation of electron equilibrium. The grid represents the medium, with letters A-F indicating regions of increasing depth. Red arrows indicate photons, which in turn, set electrons into motion. The blue arrows indicate the paths of multiple electrons and the majority of their energy are deposited towards the end of their tracks (green stars).

Dose rapidly builds in the material until a quasi-equilibrium is reached between the transfer of kinetic energy to electrons and the absorption of energy by the medium. However, the dose does not remain constant as the beam is still being attenuated as it passes into the material. Therefore, the number of photons present at greater depths is reduced, as is the transfer of kerma and, consequently, the deposition of dose decreases.

The distribution of dose as a function of depth $D(z)$ is well characterised by the *Percent Depth Dose P*, defined below, where $D(z_m) = D_m$ represents the maximum dose value, which occurs at a depth of z_m.

$$P(z) = \frac{D(z)}{D(z_m)} \times 100\% \tag{1.2}$$

An example of a Percent Depth Dose (PDD) profile for a 6 MV beam, with a field size of 10 cm x 10 cm, is shown in Figure 1.3. The curve can be described in two regions: a **build-up** region near

the surface where the dose builds rapidly until electronic equilibrium is reached and an equilibrium region where dose decreases steadily with depth due to beam attenuation.

The value of z_m increases at higher photon beam energies. Build-up regions are pronounced in beams of the megavoltage range, but not at lower energy ranges. This is because photons in the kilovoltage range, which primarily undergo photoelectric interactions, transfer less kerma to the electrons in the material and so these electrons do not travel very far. Consequently, dose is deposited into the material much closer to the site of the photon interactions. It can also be noted, from Figure 1.1, that the attenuation coefficient for kilovoltage photons is much higher than in the MV range and so more photon interaction events can be expected in the near-surface region.

As will be discussed in greater detail in Chapter 2, the presence of a high dose-gradient in the build-up region presents several challenges for the accurate measurement of surface and near-surface dose.

1.4 The Clinical Application of Bolus

In the previous section, it was shown that a beam of ionising radiation does not deposit dose evenly as it penetrates deeper into tissue. Instead, the maximum dose is deposited up to several centimetres from the surface at the depth of maximum dose (z_m). This is a great advantage in most clinical situations as this *skin-sparing effect* allows effective treatment of cancer located deep within the body.

However, it is often necessary to treat tumours close to, or on, the skin surface. This is particularly relevant in cancers of the head and neck and breast regions. In these cases, the skin-sparing effect is detrimental to the efficient delivery of dose using standard therapeutic photon beams. The skin-sparing effect can be compensated for by applying layers of tissue-equivalent material (i.e. bolus) to the patient's skin. The addition of bolus effectively shifts the PDD curve so that the build-

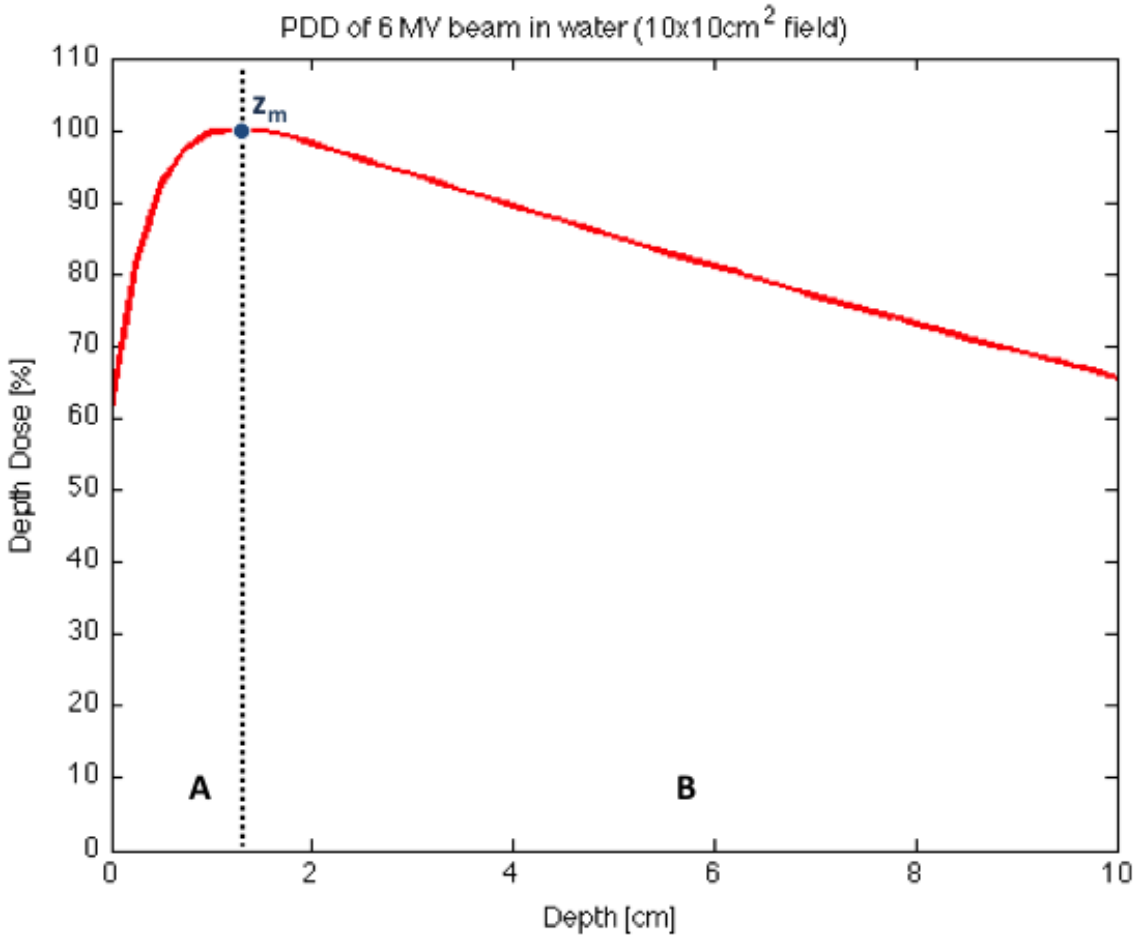

Figure 1.3: Percent depth dose curve of a 6 MV beam in water, as simulated using the Eclipse treatment planning system. Field size of the beam was 10x10 cm^2. Region A indicates the "build-up" region demonstrating a rapid increase in dose near the surface. In Region B is the dose gradually decreases with depth due to attenuation. z_m represents the depth of dose maximum, which for a 6 MV beam in water is approximately 1.5 cm

up region occurs within the additional material and the depth of maximum dose coincides with the desired clinical target. This concept is illustrated in Figure 1.4.

To be ideally suited to clinical applications, a bolus material should exhibit the following properties:

- Tissue-equivalence

- Malleability - allowing the bolus to conform to patient contours
- Reproducibility - to allow bolus characteristics to be maintained over many treatment fractions
- Non-toxic
- Cost-effective

The use of bolus is well-established and has a long history within clinical practise. In their comprehensive review of bolus materials, Vyas et.al[48], cited a report concerning the use of bolus dating to 1920. Although many different materials have been tried, ranging from rice and Play-Doh to speciality products such as Superflab^{TM}, the essential principle of adding a layer of medium on the skin to modify the dose distribution has hardly changed. It is very interesting to contrast this fact with the rapid evolution of treatment delivery in radiotherapy, even within the last few decades. From the introduction of multi-leaf collimators and inverse planning algorithms, to the delivery of high doses using increasingly smaller fields, the ability to sculpt dose distributions to match target volumes has seen dramatic progress. These techniques have significantly raised the standard for accuracy and precision in the calculation and delivery of planned dose distributions.

Interesting and clinically relevant questions present themselves when one considers the interface of modern treatment delivery and the comparatively "primitive" use of bolus. One example is found in a 2002 clinical report by Lee et.al[32]. For precise delivery of the treatment dose to target volumes, techniques such as Intensity Modulated Radiotherapy (IMRT) need to completely immobilise the patient during the course of treatment. A common method to achieve this is to place a rigid shell over the head, neck, and shoulders. This mask, shaped from thermoplast to custom fit each individual patient, is fixed to the treatment bed thus preventing movement. Lee and her colleagues observed an increase in adverse skin reactions among their patients who were immobilised in this way during IMRT treatments of head-and-neck carcinoma. To find the cause

of this skin toxicity, Lee measured the dose delivered during an IMRT treatment of the neck using an anthropomorphic phantom. Among their findings was an observed increase in skin-dose of, on average, 18% for plans carried out with the immobilisation mask compared to treatments without the mask. The authors attribute this increase in dose to an unforeseen "bolus effect" caused by the presence of the mask, which led to an increase in dose at the patient's skin, particularly in regions where the thermoplast was at its thickest.

Given the rigorous requirements for patient set-up required by modern radiotherapy techniques, the practical constraints of placing a bolus onto a patient, and the limited ability for any material to accurately conform to the contours of all patients in all treatment sites, it is not difficult to anticipate the presence of defects. Even minor differences in the thickness of the bolus, or the presence of "small" gaps between the bolus and the patient's skin may alter the shape and intensity of treatment dose distribution. Although the scale of these effects may once have been considered small, the high precision demanded by modern radiotherapy makes it clinically important to understand the limitations of commonly used algorithms in accounting for the consequences of bolus in clinical contexts.

1.5 The Effect of Bolus-skin Gaps on Surface Dose

The central focus of this dissertation is to elucidate the effects that air gaps, occurring between an applied bolus and the patient's skin, will have on the magnitude and distribution of surface dose during treatment with megavoltage photon beams. As such, it is worth presenting a brief summary of the previous literature pertaining to this issue. At time of this writing, three experimental investigations that directly address this question have been reported[13, 30, 44].

Despite the expected methodological differences in apparatus used and in the analysis of data, these studies have all come to some consensus regarding the general effects of bolus-skin gaps. All reports indicate that the surface dose is lower when a gap is present compared to the value recorded

when the bolus is in full-contact with the phantom.These papers also agreed that the magnitude of the difference depended on several factors, specifically; field size, beam energy, and the size of the air gap. Each paper found the greatest reduction in surface dose to occur for small field sizes, lower energies and large gap sizes.

To go into further details, consider the earliest of these investigations published by Butson et.al in 2000 [13]. For a 6 MV beam, 8 x 8 cm^2 field, the PDD at the surface was by 2% lower with the presence of 4 mm gap, compared to when the bolus was in contact with the phantom. This difference in PDD increased to 6% when then gap size was widened to 10 mm. However, with a field size of 10 cm x 20 cm, the change in surface PDD was only 1% and 2% for 4 mm and 10 mm gaps, respectively.

Butson's work is unique among the three studies as it also includes measurements of the influence of bolus air gaps on surface PDDs at oblique beam incidence. At larger beam angles, relative to normal incidence, the reduction in PDD caused by the presence of an air gap was found to increase; up to 10% at 60°, for 10 mm gaps and a 8x8 cm^2 fields. It should also be noted that Butson et.al did not report any significant differences in surface PDD doses occurring in the presence of 2mm air gaps. They also found negligible differences in effect between using a wax or a medi-tek bolus material.

One critique of Butson's methodology is that he analysed the effects of the air gaps by calculating the difference between the surface PDD with and without the presence of the air gap. As each PDD for each scenario is, by definition, normalized to the its own maximum dose there is no common point to compare different situations. For example, although the surface PDD for a 60° beam is 10% lower with a 10 mm gap than the case for the same beam angle without the gap, it is generally the case that PDD values are higher at oblique incidence than at normal incidence. Therefore, from this analysis, it is hard to say if the surface dose at 60° with an air gap is, in fact, any lower than at normal incidence with the same air gap.

In their 2010 study, Sroka et.al [44], attempted to look further than the simple issue of surface dose and instead investigated the effect bolus-skin gaps had on the build-up region of PDD curves for 6 MV and 15 MV photon beams. To perform this experiment they used a water tank rather than a solid-water phantom, which allowed for the dosimeter (a parallel plate ionization chamber) to be automatically scanned, step-wise, along the central beam axis and directly measure the dose curves at 1 mm resolution.

The chief purpose of a bolus is to nullify the skin-sparing effect of megavoltage photon beam. However, Sroka's results indicate that large bolus-skin gaps reintroduce dose build-up regions. In the presence of an air gap, PDD is once again observed to increase with depth and reaches 100% at a new value of z_m. Their data shows that this value of z_m increases as their air gap widens until, for very large bolus-skin distances, the value of z_m is restored to that of an open beam.

Sroka attempted to quantify the restoration of the dose build-up region by examining the dependence of observed depth of dose maximum z_m on the bolus-surface distance g. An empirical formula, describing a simple exponential relation between the two variables, was fitted to the data. However, *ab initio* justification of this relationship was offered. Sroka considered the presence of the bolus to be rendered negligible once air gap was large enough that z_m was restored to the standard value. As an example, for a 6 MV beam and 10 cm x 10 cm field, the value of z_m reached 1.5 cm for gap sizes larger than 10 cm. For 15 MV beams (same field size) the critical value of g increased to 25 cm. It should be noted that these air gaps are considerably larger than any that would be encountered in any practical medical treatment.

In 2013, Yousaf Khan [30], and his colleagues, published the results of a series of aimed at determining the effect of bolus-surface gaps on surface dose. This study was the first and, at the time of this writing, only study to expand its purview beyond simple open beams by measuring the effect of air gaps on doses delivered by the IMRT technique.

Their initial experiments, using open beam at normal incidence, agree with the general results described above i.e. decreasing surface dose corresponding to increasing bolus-surface gaps. As with Butson's findings, Khan's data shows that the magnitude of the dose reduction was found to depend on field size, with smaller fields exhibiting the largest change and the effects becoming negligible for fields larger than 15 cm x 15 cm.

Khan et.al followed this simple series of experiments by measuring the surface dose delivered to a RANDO anthropomorphic phantom during two clinically-relevant treatment plans. The first was a 5-field IMRT plan to treat the head and neck, the other was 3D-conformal treatment for the rectum using the 4-field box technique. Both plans were created using the Eclipse Treatment Planning System - Developed by Varian Medical Systems (ECLIPSE^{TM}) and each plan explicitly included the shape and location of a custom bolus. Measurements were performed using Gafchromic film. Khan's results were similar for both plans, with a 1 cm air gap reducing the surface dose by 4-6%, and a 5 cm gap resulting in a 15-25% loss, relative to the dose with no air gap.

This last point is key, as modern dosimetry is increasingly becoming a more computational science. Algorithmic dose calculations are vital component in both treatment planning and post-treatment quality assurance. Although the effect of a bolus air gap on surface dose has been broadly described by the experiments described above, to our knowledge, no attempt has been made to study this specific phenomenon using computational methods. Therefore, a comparison of experimental and simulated data regarding the effects of air gaps in bolus is value to the medical physics community, and it is here that have aimed our investigation.

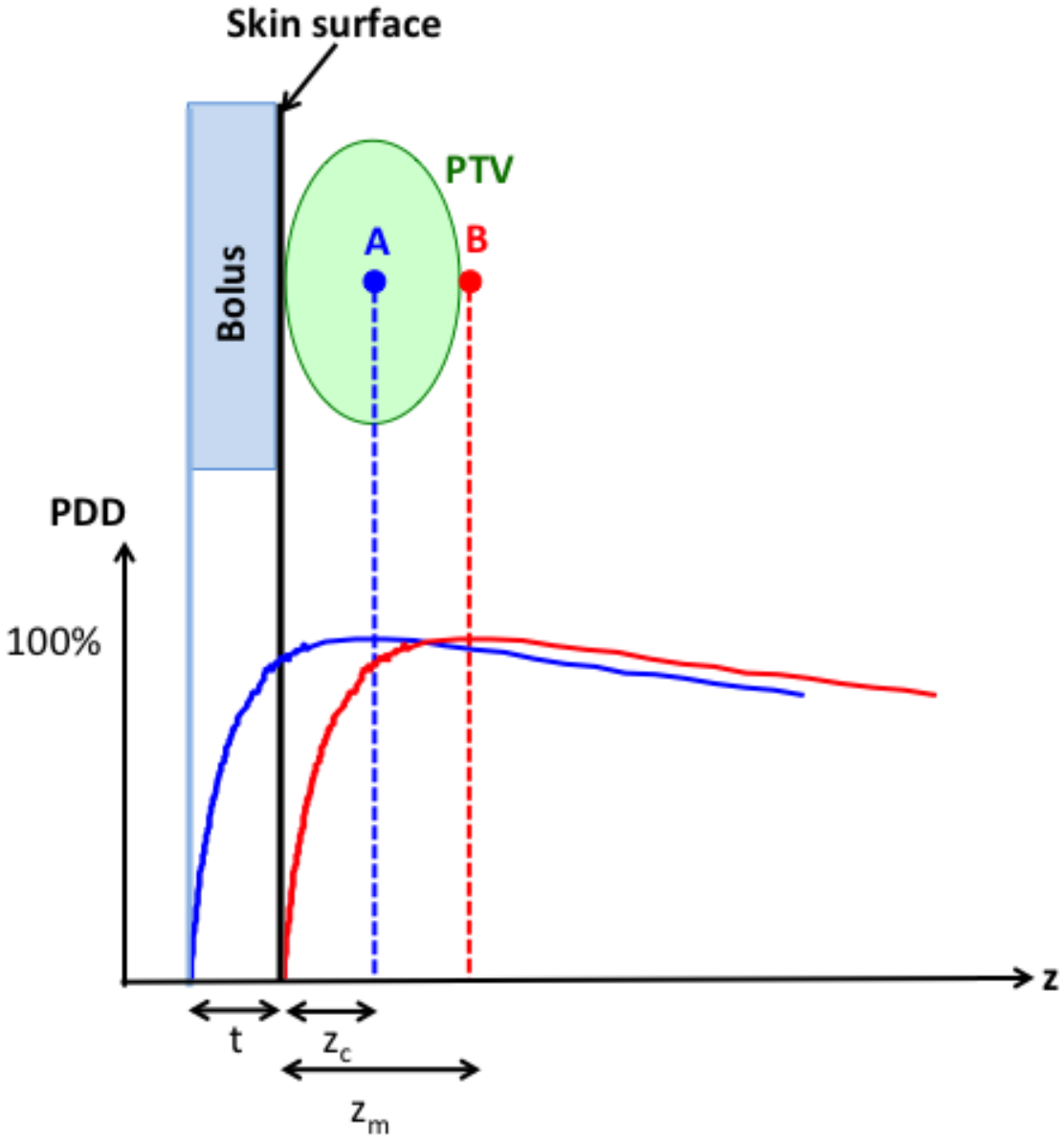

Figure 1.4: A schematic illustrating how bolus can be used to achieve more efficient deposition of dose into the Planning Target Volume (PTV). The maximum dose should, ideally, be deposited in the centre of the PTV at depth z_c (Point A). Without the use of bolus, the dose will be distributed according to the red PDD curve. In this case, it is clear that the maximum dose will miss the PTV and will instead coincide with point B. However, if water-equivalent bolus of thickness t (blue rectangle) is added to the surface, the PDD will be shifted as shown by the blue curve. Now the depth of maximum dose will coincide with point A, as desired. The thickness t can be determined as $t = z_m - z_c$

Chapter 2

Experimental and Simulated Dosimetry

2.1 Introduction

One of the key challenges facing the clinical medical physicist is the accurate and reliable measurement of radiation dose. As we discussed in the previous chapter, the term "dose" quantifies the eventual absorption of energy into tissue after a series of successive interaction events. Given the various ways that the original energy is spread, transferred and transformed, directly measuring its absorption into the material would be impossible. For example, if it was possible to determine the location and quantity of energy absorbed from the photons, this would still be insufficient as that energy would continue to spread through the release of electrons.

To measure dose in an experiment, we must rely on the use of instruments and materials that display a pronounced response to radiation, such as the build-up of charge, the release of luminescent photons, or the triggering of a chemical reaction. The response must then be carefully calibrated so that the energy absorbed can be determined from the observed response. However, each of these dosimetric methods come with a number of caveats and contingencies to be aware of. For example, many of these materials are distinctly different from tissue in terms of physical and electron density and, therefore, require care in generalizing the results to clinical contexts. Other

methods are only applicable in certain dose ranges, or have physical limitations in terms of their size or orientation.

However, with the power of modern computers, many have attempted to directly access the subatomic processes underlying the transfer of dose by creating extensive simulation of particle interactions. These computerised methods of dosimetry are now the foundation of modern treatment plans, where algorithms are used to optimise calculated dose distributions, aiming to make the results of each successive calculations better than the previous one. These techniques range from empirical models that simulate the spread of dose deposited by *beamlets* of radiation, to full-scale probabilistic simulation that track the interaction history of millions of virtual particles.

In either case, a thorough understanding of your dosimeter of choice, including the mechanism of its operation and its limitations, is necessary to provide suitable context for any discussion of the results. For that reason, this chapter aims to provide a brief overview of the specific techniques used in this investigation. Our discussion will be focussed upon the methods used in our work i.e. the use of parallel plate ionization chambers, radiochromic films and Monte Carlo calculations. As the results of our experiments and simulations will be compared to dose values obtained using the Analytical Anisotropic Algorithm (AAA), as employed by the ECLIPSE^{TM} treatment planning system, we will also touch on convolution methods for calculating dose. The review provided in this chapter is by no means exhaustive, it is intended only to provide useful context for the description of our research methods and results. However, the references cited in these pages would provide an excellent framework for any who wish to understand these techniques in greater detail.

2.2 Experimental Dosimetry

2.2.1 Ionization Chambers

To begin our review of dose measurement, it is useful to define two terms that are often used to categorise dosimetry techniques:

Absolute Dosimetry Refers to measurements that provide a direct value of the energy absorbed from a radiation source, such as a measured increase in temperature (calorimetry) or ionization charge. The value of dose is then given in reference to a recognised, external standard and in a standard unit, usually Gray [Gy]. In our experiments, we perform surface dose measurements using a Markus Parallel Plate ionization chamber. Certain ionization chambers fall into the category of *Absolute Dosimeters*, and are the basis of the TG-51 protocol, the standard means of characterizing a treatment linac. However, although this instrument can be used to obtain exact dose values in Gy, for the purposes of our experiment (as will be discussed later) we have used it as a relative dosimeter.

Relative Dosimetry These measurements rely on some observed characteristic that can not be directly/mechanically linked to the absorption of energy, but whose response to radiation can be well-established. Relative dosimetry relies on the use of a calibration curve, where measurements of the response to known exposures of the photon beam can be used to estimate an unknown dose. Gafchromic film is an example of a Relative Dosimeter. By calibrating the change in optical density for several films exposed to known doses of radiation, the unknown dose absorbed by a test film can be estimated from its optical density.

When matter is exposed to radiation the atoms/molecules within the material become ionized. For the typical range of pressure and electron energies likely to be experience in a clinical setting, the average energy required to produce a single ion pair in air is approximately constant and is

equal to $W = 33.97$ eV/ ion pair. Therefore, the energy transferred from the radiation beam to a volume of air is directly proportional to the measured ionization charge. From this fact, an absolute dosimeter can be constructed with two parts: an *Ionization Chamber*, where a well-defined volume of air is ionized by exposure to a radiation beam, and an *Electrometer* for collecting and measuring the resulting charge.

Of course, the reality is more complicated than the simple idea described above. In Chapter 1, it was established that the deposition of dose from a photon beam is a two-step process. As such, the ion pairs measured within the chamber are unlikely to be the product of photon interactions within the gas, but are instead the results of energy lost from electrons originating within the walls of the cavity. Therefore, the dose value ascertained from the measurement of charge within the gas must be related to the dose absorbed by the cavity walls by a conversion factor (the ratio of stopping powers for the gas and the wall materials).

Even once the dose absorbed by the cavity wall's has been established, clinical applications require a measurement for the dose that would be absorbed by patient tissue rather than wall material. Fortunately, it is possible to convert the dose absorbed by the walls to that which would have been absorbed by a volume water-equivalent medium (the typical approximation for tissue) if it were in the cavity's place. This conversion factor is derived from a ratio of the energy absorption coefficients for the gas and water, i.e. the relative abilities for these materials to absorb energy through photon interactions. However, the applicability of these conversions requires two assumptions: Firstly, that the chamber walls are thick enough that electrons creating ion-pairs within the cavity could only have originated from the walls and not from the surrounding medium; and secondly, that a condition of electronic equilibrium exists. This latter criterion is necessary to directly relate the energy transferred to the walls/medium from the photon beam (i.e. the Kerma,) with dose absorbed.

The preceding paragraphs begin to illustrate some of the challenges involved in accurate clinical dosimetry. Even with a well-characterised response to energy deposition, such as the creation of ion pairs in air, a number of corrections are needed to relate the behaviour of a measurement device in a experiment to that of human tissue in a clinical situation. Other correction factors, in addition to the chamber wall correction alluded to above, include[8, 26]:

Replacement Correction To account for the perturbation in electron fluence caused by the presence of the cavity and any resulting shift in the precise point of measurements within the chamber.

Electrode Correction To account for differences in material between the chamber walls and the collecting electrode.

Air temperature-pressure Corrections Accounts for differences in environmental factors between laboratory and calibration conditions.

Ion recombination Corrections Some ion-pairs that are created by the radiation will recombine before they are collected, therefore their charge is not measured, and that energy is effectively"missed" by the detector. A correction factor can be applied to account for this loss.

Polarity Corrections The response of the dosimeter (the paired ionization chamber and electrometer) can differ depending upon the polarity of the bias applied to the chamber. A correction factor to compensate for this difference may be required.

The necessity of these correction factors can make ionization chamber dosimetry appear "dubious". However, there exist established methods for accurately determining these corrections. Careful application of these techniques, using an externally calibrated dosimeter, will result in accurate measurement of absolute dose. For a a thorough discussion of these procedures the reader is referred to the AAPM's TG-51 protocol [8], and to the following texts[26, 29].

As our investigation used a ionization chamber as a relative dosimeter, most of these correction factors were not needed and discussion of those that were applied is reserved for the discussion of experimental methods in Chapter 3. Instead, we turn to the use of ionization chambers for measurement of **surface dose**.

2.2.2 Parallel-Plate Ionization Chambers

A major challenge facing the use of ionization chambers in surface dosimetry is the absence of electronic equilibrium, which is a necessary condition to clearly relate the measured dose in the chamber to dose in the medium. Another issue is the fact that surface or skin dose is a quantity defined at a specified plane, whereas ionization chambers collect charge from throughout a volume. In fact, the International Commission on Radiological Protection (ICRP) recommends measuring skin dose at 70 μm from the outer surface, which corresponds to the depth of the basal layer of the epidermis [39]. This depth is far to shallow to be commensurate with a practical collection volume for a chamber.

Despite these issues ionization chambers are still used for surface dosimetry. They use a Parallel-plate (PP) geometry, as opposed to the more typical cylindrical set-up. The advantages of the parallel-plate design is that they can be constructed using thin foils as electrodes, which minimizes attenuation and scattering of photons as they pass into the cavity. They also allow thin gas layers to be as used as the collection volume, allowing for greater depth resolution. Extrapolation PP chambers allow the thickness of the gas layer to be adjusted allowing a series of measurements at different "depths" from which the dose at 70 μm can be extrapolated. These extrapolation chambers are generally considered the most accurate method of skin dosimetry. Unfortunately, a large number of measurements are required to create the curve from which skin dose can be extrapolated, which limits their practicality in clinical environments.

Another option is to use PP chambers with thin, but fixed, collection volumes. However, these instruments come with some unique design concerns and some additional complications. Figure

2.1 below shows a simplified schematic of a fixed-separation PP chamber. From this image, the PP is seen to bear some resemblance to a parallel-plate capacitor. As with the capacitor, the electric field between opposing plates is not strictly aligned normal to the plates as their may be "edge effects". All ionization chambers determine dose by collecting the charge liberated from a precisely define volume of air, and so, any bending of the field at the edges will alter this volume and affect the dose values measured. To counter this effect, most PP chambers include a "guard ring", which is a ring of conducting material surrounding the collection electrode. The guard ring is held at the same voltage as the collection electrode, so effectively extends the electric field beyond the define limits of the collection volume and shifting the edges away. However, the guard ring is electrically insulated from the collection electrode and so does not contribute to charge collection.

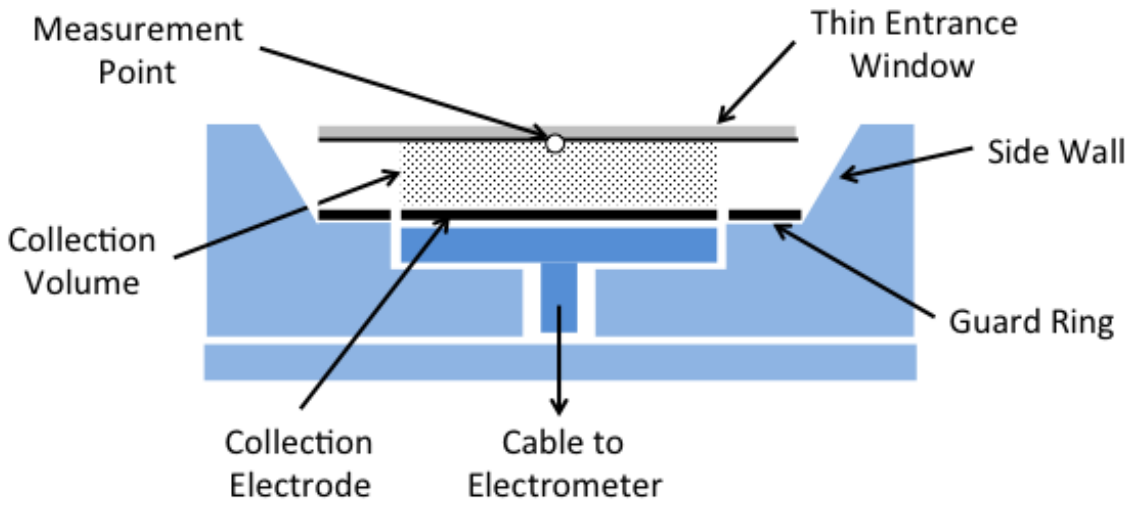

Figure 2.1: A simplified schematic showing the key design features of a Fixed Separation Parallel Plate Ionization Chamber.

As can be seen in Figure 2.1, the photon beam passes directly through the collection electrode of the PP chamber. Therefore, photon interactions will occur within the electrode itself and electrons may be "kicked" out via the Compton Effect. The loss of these electrons will result in an additional positive current being introduced into the electrometer and will result in inaccurate

dose measurements. This effect is most pronounced in chamber designs featuring thin entrance windows, thick collection electrodes and small separations between plates. A standard method for accounting for this issue, which we have employed as noted in Chapter 3, is to measure the charge multiple times at both positive and negative electrometer bias and then average the results to obtain the final estimate of charge.

One significant characteristic of PP chambers is their well-known tendency to overestimate Percentage Depth Dose (PDD) in the build-up region. Increased ionization due to secondary electrons released from the chamber walls is generally considered to be the principle cause of this effect. In their 1985 paper, Nilsson and Montelius proposed several recommendations regarding the design of chambers used for dose measurements in non-equilibrium conditions [35]. These suggestions included: the use of large (relative to plate separation) guard rings to reduce the influence of side-wall electrons, and large side wall angles (relative to the beam axis) which would increase the absorption of secondary electrons within the walls.

However, in addition to these design concerns, it is necessary to apply an empirically derived factor to correct PDD measurements obtained using PP chambers. In 1975 Velkey et.al, proposed a series of corrections for application in the build-up region, by comparing the results of a fixed-separation PP chamber to an extrapolation chamber [47]. However, these factors proved to lack generalizability as their results could not be accurately applied to chambers of different designs. In 1989, Gerbi and Khan expanded upon Velkey's work by accounting for additional geometric factors such as the distance between the side walls and the collection electrode, and obtained corrections for several commonly used chamber designs and photon energies[25]. Their method has been utilized in many subsequent studies [9, 10, 37] and is the approach we have adopted in our investigation. The correction formula are presented in more detail in Chapter 3.

Each experimental method used to determine dose has strength and weaknesses regarding its application. Although ionization chambers are considered the gold standard regarding accurate

absolute dose measurement, the above discussion makes it clear that they are not without flaws, especially when measuring dose in the build-up region. Therefore, it is always good practise to utilize a second technique (or even more) to corroborate dose measurements. In particular, as modern radiotherapy techniques allow for shaping' dose with increasing precision, the ability to measure the "distribution" of dose is vital. This feature is the key strength of using Radiochromic films in dosimetric experiments, and we shall now discuss this methodology.

2.2.3 Radiochromic Film Dosimetry

The use of radiochromic (sometimes known as GafChromic) film has much in common with photographic films. In fact, some of the earliest films used for dosimetric purposes were coated in a silver-halide emulsion like those used for black and white photography. As with photographic films, radiochromic films are sheets of radiosensitive material that undergo a chemical reaction when exposed to radiation.

These chemical changes effect the transmission of light through the film. Usually the intensity of light passing through the exposed film is reduced, rendering it more opaque than the unexposed regions of the film. In the case of the EBT3 films used in this study, radiation triggers the polymerization of di-acetylene monomers in the films active layer. The change resulting in transmission can be related to the radiation dose absorbed by the film. The opacity of the film is usually quantified by the its **optical density** (OD) according to equation 1, where I represents the intensity passing through the film and I_0 is the intensity of the light source in the absence of film.

$$OD = \log_{10}\left(\frac{I_0}{I}\right) \tag{2.1}$$

Of course, for dosimetric purposes the quantity of interest is the change in optical density caused by exposure to radiation. This can be computed from the intensities of light transmitted through the exposed I_{exp} and the unexposed I_{unexp} film as shown in Equation 2. Measurements of

OD were traditionally performed with an optical densitometer, which was essentially a coupled light source and photoelectric cell. The film would be "sandwiched" in between the pair, and the photocell would measured the intensity of light from the source that was transmitted through the film. The more modern method is to use a high-resolution flatbed scanner to perform transmission measurements on the whole film sheet simultaneously, with high transmission corresponding to a high (or "bright") pixel value in the scanned image.

$$\Delta OD = OD_{unexp} - OD_{exp} = \log_{10}\left(\frac{I_{unexp}}{I_{exp}}\right) \tag{2.2}$$

Unfortunately, the relationship between a film's change in optical density when exposed to radiation and dose is not consistent or well-characterised and can depend on a number of factors will be discussed below. Therefore, radiochromic films are a tool for relative dosimetry and must be well-calibrated to yield useful measurements of dose. Calibration curves are produced by exposing pieces of film to known doses and fitting a response curve describing the relationship between dose and the observed change in OD. This curve is then used to infer unknown dose values from the optical density of test films.

Further information on film calibration can be found in Chapter 3, where the calibration procedures used in our experiments are discussed. For the remainder of this section, we will outline some of the factors that can effect the dose response of film, and review the work pertaining to surface dose measurement with films that can be found in the literature.

2.2.4 Factors Effecting Dose Response in Film

The response of a given sample of radiochromic film to a given radiation dose is, in some ways, unique to that particular sample. Although it can be presumed that a hypothetical element of the photosensitive material would respond to a given quantity of energy according to some mathematical relationship. In reality, the photo-polymerization process is sensitive to a large number of

confounding factors relating to the manufacture of the film, the context of the experiment in which the film is exposed to radiation, and to the conditions and method by which the optical density is quantified and calibrated against dose. For a detailed discussion of these factors we recommend the review by Devic et.al [23] and the manufacturer's documentation for the EVT3 films[3]. However, we will provide a brief summary below.

Time-Dependence Photoinduced chemical changes in the film material are not instantaneous processes. Once triggered by exposure to radiation, the reaction is initially quite rapid, but the rate gradually slows[40]. Clearly, OD measurements that are taken too early, i.e. as the reaction is still proceeding, will not accurately reflect the response and will lead to an underestimation of dose. Although a dose error of ¡ 1% can be achieved within 30 minutes of exposure [22], scanning films after at least 24 hours is the commonly accepted practise.

Energy-Dependence The response of a film to a given level of dose can vary with beam energy depending on the chemical composition of the active layer. EBT3 films have been shown to under-respond at low energies (¡ 50 keV)[15, 40]. However, they demonstrate no significant energy dependence in the megavoltage ranges typically used for medical applications.

Film Orientation For photo-polymerizing films such as EBT3, the active layers consists of long, "needle-shaped" monomers whose long axes are aligned along a particular film axis. The asymmetric shape of these particles will result in anisotropic light scattering within the film. This will have a strong effect when scanning the film data with a flatbed scanner. Therefore, it is important that all film samples are scanned in the same orientation so that accurate dose comparisons and calibrations can be made.

Batch variance Small variances in the manufacture of radiochromic films, such as slight differences in the thickness of the active layer, can result in notable differences in dose response[23]. Films obtained from one batch may display significant under/over response compared to an-

other batch. Consequently, comparisons of optical density cannot be made between samples from different batches. Therefore, each film batch should be separately calibrated and that experiments utilise films from the same batch so that accurate comparisons can be made.

These are, by no means, a full list of possible conflicting factors that can influence the use of radiochromic films as dosimeters. Environmental factors and exposure to ambient light can also have an affect. Therefore, when considered as "pure" dosimeters, they are not the most ideal instrument to use. If **exceptional** care is taken in controlling these factors, errors of ¡ 5% can be achieved [23]. However, in terms of spatial resolution, films are vastly superior to most other dosimetric methods. The radioinduced polymerization of the film material is a very localized effect, which allows the film to capture a map of dose intensity and distribution. This is similar to how photographic film maps visible light intensity to create an image. The advantages of taking a "dose image" are hard to overstate given the critical role that controlling the shape of dose-distributions play in modern radiotherapy. This ability is they key reason why we have chosen to use radiochromic films in our research, as we shall be mapping the changes in dose distribution caused by bolus-skin gaps (Chapter 5).

2.2.5 Films for Surface Dosimetry

At first glance, radiochromic films would seem like an ideal instrument for measuring surface dose, assuming that the various confounding factors could be controlled. They are thin, flat sheets that can be placed directly upon the surface and provide measurements in a 2D plane. They are also composed of an organic polymer material that dosimetrically comparable to water. However, as with ionization chambers, and most other dosimetric methods, the challenge of measuring accurate skin dose with film stems from the rapid build-up of dose in the first few millimetres of phantom depth.

As thin as they are, the measurement depth (i.e the location of the active layer) of a radiochromic film is typically hundreds of μm from the films surface. As an example, the effective measurement depth of the EBT3 films used in our investigation was determined to be 0.0189 g/cm^2. This is greater than twice the depth of the ICRP defined skin depth of 0.007 cm. Given the high dose gradient in the build-up region, a difference in depth of even tens of μm can lead to an notable over-estimate of dose.

A comprehensive study to quantify this effect, and to suggest possible correction factors, was published by Devic, Seuntjens, and colleagues in 2006[21] . In their study they compared the surface doses, measured with three models of radiochromic films (EBT, XR-T and HS), with references PDD obtained using an extrapolation chamber, an Attix parallel-plate chamber and Monte Carlo (MC) simulations. In addition, Devic et.al. also performed similar measurements on exit doses to determine the accuracy of radiochromic films when applied to the surface through which the treatment beam leaves the phantom.

Their results demonstrate that, due to the difference in the effective point of measurement, surface doses measured using radiochromic films do not accurately reflect "skin dose" i.e. dose at 70 μ depth. For example, for a 10x10 cm^2 6 MV field, their EBT films measure a surface PDD of 19.9% compared to the "true" skin dose of 17%. Therefore, to estimate an accurate skin dose value using EBT film would require a correction factor of 0.854. These correction factors show some dependence on field size, as films appear to overestimate dose to a greater degree at smaller fields.

Another method to obtain accurate surface doses with films is due to Butson et.al, who proposed using extrapolation determine dose an effective depth of 0 mm [12]. Extrapolation chambers, which are still considered the most suitable tool for surface dose measurement, require a large number of individual measurements, at different plate separations, to create the extrapolation curve. However, films do not suffer this disadvantage as numerous film strips

can be exposed simultaneously. By arranging five film pieces into a "stack", Butson and his colleagues were able to take central-axis dose measurements at multiple depths within the first millimetre of the build-up region. A quadratic function was fitted to the film data points to produce an calibration curve that was be extrapolated to estimate dose at approximately zero depth. Their extrapolated surface PDD for a 10x10 cm^2 field was 15$\pm$2%, which was in good agreement with a reference value of 16$\pm$1% taken with an Attix PP chamber. It is worth noting that this reference value represents a measurement from an uncorrected PP chamber, and so the difference between the chamber and film extrapolation values could be larger given the established tendency for PP chambers to overestimate surface dose. However, further measurements within the same article, taken at several field sizes and with both open and perspex-blocked beams, indicated that film extrapolated surface dose values were generally with 2% of corrected Attix measurements.

In 2004, Butson followed this work using radiographic films and extended the method to produce two-dimensional surface dose profiles using extrapolation [14]. Once again the extrapolated surface doses agreed within 3% of value obtained using an Attix PP chamber. In 2009, Chiu-Tsao and Chan [18] published a similar, but more methodologically detailed detailed, report on the use of radiochromic film stacks for measuring build-up dose with high depth resolution, and the extrapolation of surface dose estimates. They reported a surface PDD of 15$\pm$0.7 %, which is in good agreement with Butson's work. This paper is also worth noting as it provides a table summarizing the reported values of central-axis surface dose for 6 MV, 10x10 cm^2 beams, which may be of interest to the reader.

The above discussion serves to provide a sufficient background into the experimental methods used within this thesis. However, modern dosimetric is an increasingly computerized process and our focus shall now shift to consider computational methods of determining patient dose.

2.3 Computer Simulated Dosimetry

As in the previous section, our discussion shall focus on the dose calculation methods most relevant to our study of the bolus air-gap effect, i.e. Monte Carlo Simulations and the AAA. The latter method is an algorithm created by the Varian corporation for use in their Eclipse^{TM}Treatment Planning System. Although other algorithms may be employed within this system, we shall only consider the AAA and so the terms AAA and ECLIPSE^{TM} can be considered equivalent within this thesis.

As with most areas of science, Medical Physics has benefited tremendously from the power of computation. Dose calculation programs allow for more sophisticated treatment plans than would be feasible for humans to perform accurately and without error. Computers are now at the heart of modern radiotherapy, and have made possible much of the rapid progress in treatment delivery methods. Techniques such as Volumetric Modulated Arc Therapy (VMAT) shape the distribution of dose to match the prescribed Planning Target Volume (PTV) by using optimisation algorithms to determine the appropriate treatment delivery parameters.

The most accurate method of calculating dose is to model the behaviour of millions of photons, electrons and other particles as they spread through the medium. MC simulations perform this task stochastically through repeated random sampling, as shall be discussed in detail below. However, this approach requires significant computational resources that have only recently become commonly available. A more efficient approach is to model the dose using analytical and empirically-derived functions, and then building upon these by applying various corrections until a more realistic representation of the treatment is achieved. The AAA is one of several examples of the latter approach, which have proven to be reliable and robust and are used in most treatment planning cases. However, an approximate approach is only as valid as its underlying assumptions, and the accuracy of these calculations can suffer

in situations where these assumptions no longer hold, as in non-equilibrium regimes like the near-surface region.

2.3.1 The Analytical Anisotropic Algorithm

Before discussing the AAA in detail, it is worth discussing how a materially accurate representation of a patient or phantom can be introduced into a computer program. The subject is described by a three-dimensional array that serves as a "3D image". As a common 2D image is analogous to a matrix whose member values represents the intensity (brightness) of each pixel, the elements of the 3D array record the mass density of the subject medium. Therefore, the variation of tissues present in the human body are encoded within the changes of density value across the array. The resolution of this model, how smooth and precise the separation between tissue types can be delineated, is limited only by the geometric size of each element, which are called *voxels*.

It should be noted that much of the following overview of the AAA is based upon documentation written by Janne Sievinen of Varian Medical Systems, developers of the ECLIPSE^{TM} TPS [43].

The role of the dose calculation algorithm is to bridge the gap between the predetermined beam fluence and the resulting dose to the medium. As stated in Chapter 1, the principle difficulty in relating the properties of a photon beam to dose is the fact that dose is not deposited at the location of photon interactions. Whereas MC would simulate the paths and interactions of the secondary electrons stochastically, algorithms such as the AAA approximate the spread of dose by using the mathematical properties of *convolution*.

The general concept behind this approach may be familiar to those well-versed in the behaviour of simple filters and transformations such as those used in medical imaging. At a high-level, the medium can be considered as a system that takes a certain input, the energy

transferred from photon interactions, and processes it to produce an output, dose. A well-known result from the theory of such transforms is that the output signal can be represented as the convolution of the input signal with the systems *impulse response*. The impulse response is the systems output in the special case of an input signal that is infinitesimal in size and duration e.g. a point source. In our analogy, such a signal corresponds to the total energy transferred, from the beam, into a single voxel. The resulting spread of dose into the surrounding voxels forms the impulse response, which is approximated by analytical functions called *scattering kernels*.

This use of convolution as a means to calculate dose is the foundational element of AAA and many similar methods. Computers can perform very rapid convolutions using Fourier Transforms, making the approach extremely efficient and fast-enough for routine clinical use. Therefore, a large portion of the "work" in these programs is dedicated to approximating the properties of the linac in terms of familiar functions (such as linear combinations of Gaussian or exponential curves) that are amenable to convolution. The main "selling point" of the AAA in particular, is the use of detailed MC simulations and experiments to establish a database of information, which is then used to scale and correct the functions according to each specific clinical situation.

Determination of these empirical functions is performed by a process within the AAA called the *configuration algorithm*. The configuration algorithm recreates the properties of a specific treatment unit, specifically the fluence and energy spectra of the photons and electrons composing the beam. These parameters are derived from both experimental measurements and MC simulations. MC is used to determine baseline information such as the photon energy spectrum and the beam intensity profile, then these functions are adapted to match dosimetric data as measured in a water-equivalent medium. The initial MC simulations are performed using a detailed virtual recreation of a given linac, and the experimental results also come

from the same machine, therefore the modelled beam is specific to that unit. The resulting parameters are stored and retrieved during treatment planning for use in the dose calculation algorithm. The parameters of the kernel functions are also determined by MC and adjusted to the clinical setting according to the stored characteristics of the beam, and the physical properties of the medium.

As the patient is represented as an array of individual volume elements, so the treatment field is considered as composed of smaller, linear elements called *beamlets*. Ray-tracing is used so that the boundaries of each beamlet are commensurate with the angle of beam divergence, and the voxel of the patient are redrawn to match. The properties of each beamlet are then determined from the parameters established by the configuration algorithm and tailored to accurately describe the given clinical context. In the AAA, each beamlet is actually composed of three parts representing the primary photons generated from the beam source, the extra-focal photons produced by the flattening filter or collimators, and the electrons present in the beam.

This information is then used to determine a function estimating the total energy released in each voxel along the beamlet path. This is our "input" signal, which is then convolved with the appropriate scattering kernels, across the whole phantom, to determine the distribution of dose.

An important feature for any clinical dose calculation program is the ability to accurately account for the heterogenous nature of human tissue. A radiation beam passing through a patient's chest may encounter numerous inhomogeneities such as; regions where the anatomy results in areas of varying tissue thickness (e.g. a field partially covering a patient's breast), or structures with higher (bones) or lower (lung) electron density. Although, computational efficient the use of simple functional forms to model the behaviour of a treatment field in tissue can encounter difficulties in adapting to changes in anatomical density. The AAA ad-

dresses this challenge by rescaling the properties of each beamlet, and those of the scattering kernels, according to the local density [43]. For example, the dependence of a given functional form on the depth z is reparameterised in terms of the radiological depth z' according to:

$$z' = \int_0^t \frac{\rho(t)}{\rho_{water}} dt \tag{2.3}$$

There is some disagreement within the literature regarding the effectiveness of this correction method based. Several studies have indicated that the AAAs treatment of inhomogeneities provide satisfactory accuracy in determining dose [43, 46]. Others have indicated notable discrepancies [7, 41]. The interests of our work focus on the treatment of surface doses and extreme inhomogeneities (i.e. air gaps). However, all of the published investigations relevant to that topic use MC as a 'gold-standard" reference in determining the accuracy of their AAA results. Therefore, it is worth briefly discussing the MC method before considering these studies.

2.3.2 The Monte Carlo Method

In physical systems, many of the properties than can be observed, measured and treated mathematically actually arise from the random actions of particles on the atomic or molecular scale. For example, changes in temperature or the diffusion of a gas through a volume both originate in the random motion of particles driven to seek a lower energy state. As shown in Chapter 1, the dose deposited by radiation into some medium is also a gross quantity that is a consequence of the random interactions of billions of photons and electrons. However, whereas temperature changes or diffusion can, in some cases, be treated using well-known differential equations, the transfer of dose does not lend itself to a straight-forward analytical treatment. In cases such as these, the power of computation can be harnessed to simulate

the underlying random events directly and properties such as dose are determined through averaging the "lives" of millions of simulated particles.

Algorithms that make use of random samples to solve intractable mathematical problems are generally known as **Monte Carlo Methods**, after the famous casino in Monaco. In these methods the history of some element, say a particle, from its generation to its eventual absorption into the medium is entirely determined by the "roll of a die", or more accurately by a random sample from the appropriate probability distribution. To provide a more concrete example of this method, we shall consider how the movement of a particle might be determined in a typical MC simulation.

Consider a photon of energy E, moving in a given direction through a medium with absorption coefficient $\mu(E)$. The probability of this photon travelling a small distance x before undergoing a random interaction process is given by:

$$p(x) = \mu(E)e^{-\mu(E)x} \tag{2.4}$$

Given this, the probability that the photon will travel any given distance between 0 and x is given by the *cumulative distribution function*, which can be obtained by simple integration.

$$P(x) = \int_0^x mu(E)e^{-\mu(E)x}dx = 1 - e^{-\mu(E)x} \tag{2.5}$$

At this point in our simulation we can obtain a suitable "guess" for the value of $P(x)$ by generating a random number R from within the range $0 < R \leq 1$ i.e:

$$R = \int_0^x mu(E)e^{-\mu(E)x}dx = 1 - e^{-\mu(E)x} \tag{2.6}$$

From this relation we can determine the distance our simulated photon will move commensurate with the randomly supplied probability R.

$$x = \frac{1}{\mu(E)} \ln(R) \tag{2.7}$$

The coordinates of the photon within the medium are then updated such that it can be considered to have moved a distance x along its original direction of motion. Having reached its new location we can determine which interaction it will now undergo using another "dice toss".

As can be seen in Figure 1.1, there exists a comprehensive body of empirical data relating the probability of a given interaction event (as measured by the mass attenuation coefficient σ) with the photon energy. The probability of, say, a Compton Scattering interaction occurring rather some other mechanism can be determined from this data as follows:

$$p_C = \frac{\sigma_C}{\sigma_{total}} \tag{2.8}$$

Where σ_{total} is determined from the sum of the mass attenuation coefficients for all relevant interactions. We can map the probability of an interaction onto a range between between 0 and 1 as shown schematically in Figure 2.2. In essence, the probability space is split into "bins" whose relative size depends upon the energy of the photon and the attenuation properties of the material. Once again a random number $0 < R \leq 1$ is generated and the bin this number lands in determines the interaction event undergone by the photon.

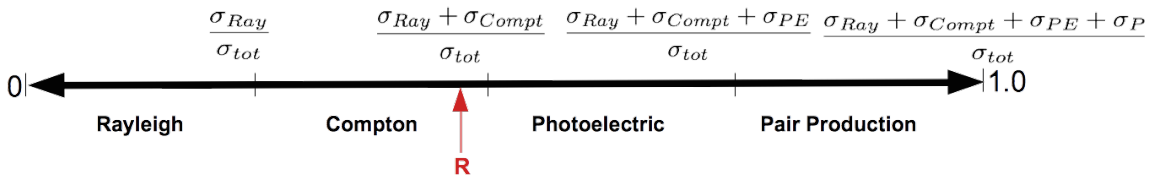

Figure 2.2: A schematic illustrating how mass attenuation data can be mapped into a probability in the range $[0, 1]$. MC algorithms use a randomly generated number R, whose place in this range is used to determine the interaction of a simulated photon.

The above discussion illustrates the key mechanics of how random number can be used to simulate the physics of photon transport in a medium. This process is repeated in various forms to recreate the "history" of a given photon. In scattering events, the new direction of the photon can be randomly determined in line with established theory such as the Klein-Nishina formula. In Pair-production or Photoelectric interactions, the simulated photon can be "terminated" after triggering the production of simulated electrons whose behaviour are also modelled as a succession of random processes. With modern computer power, the lives of millions of virtual particles can be recreated. After each event, the energy transferred from each particle to the medium is recorded. Therefore, by averaging over a sufficiently large number of the distribution of dose in the medium can be accurately calculated.

The applications of this method are vast as it models particles transport directly using readily available material properties such as absorption coefficients and cross-sections. With sufficient information regarding the geometry and materials of the machine, a virtual model of the treatment linac can be constructed. Therefore, MC can accurately reconstruct the behaviour of an actual radiotherapy unit in clinical use, rather than requiring an approximation of a treatment beam. Similarly, using tissue density information available through high-resolution medical images (such as a CT scan) an accurate 3D model of a patient can be constructed for use in MC simulations. With accurate modelling of both the linac and the

patient, MC can be used to calculate and predict dose distributions for individual treatment plans.

Accurately recreating the history of single particle, through multiple steps of translation, interaction and energy transfer processes, requires a substantial number of individual calculations. When this processes is repeated for the large number of particles necessary to produce a statistically accurate model, the process quickly becomes "expensive". The high cost of these simulations is the primary weakness of MC methods. The time taken for to complete a simulation makes makes the method impractical for use in routine treatment planning. Even with access to a distributed computer network, computation time can still be significant, and competition for limited computer resources between treatment plans can exacerbate this delay. Of course, not all institutes have access to such computing clusters. For smaller and more remote centres and hospitals in the developing world regular use of MC simulations are near impossible. As such, more approximate but computationally tractable methods such as AAA still have a major role in radiotherapy.

At the point a clear distinction between MC simulated linacs and their real-world counterparts must be made. In the MC algorithm, the number of particle histories, whether millions or billions, has no relation to the properties of the simulated beam. In real linacs the intensity or duration of the treatment, and thus the dose delivered, is related to the rate and number of electrons striking the target at the beam source. For MC beams, a larger number of histories produced greater statistical accuracy but does not map to the properties of the beam. Therefore, it is not a simple task to determine absolute dose values using MC.

However, Popescu et.al published a method for calculating absolute dose with MC in 2005[38]. A key aspect of their approach was their choice of the BEAMnrc and DOSXYZnrc codes, developed by the National Research Council of Canada, to perform their simulations. After performing a dose calculation, these programs normalize their estimated dose values by the

number of initial histories, essentially reporting the dose produced per particle. Therefore, it is possible to determine absolute dose provided the dose at any given point in the medium can be related to the initial number of particles. Unlike experimental dosimetry, MC simulations provide complete freedom upon where you choose to "score" the dose, and so Popescu was able to calculate the dose (per particle) to the monitor chamber of his virtual linac. As the dose to the monitor chamber is used to define the linac's Monitor Units, a relationship between the number of particle histories and monitor units could be established. In clinical environments, the TG-51 protocol is used to empirically determine the relationship between dose to a set reference point (in water) and a linac's monitor units. Popescu and his colleagues recreated the benchmark tests of the protocol using MC, effectively calibrating the virtual linac, determining the dose per monitor unit. Combining all of these elements a simple conversion factor was derived, allowing absolute dose at a given voxel to be predicted from the prescribed monitor units of simulated treatment plan.

The 2005 paper by Popescu et.al, it also especially relevant as the work was performed at the BC Cancer Agency's Vancouver Centre. The methods described in this article form the foundation of the MC system currently used for treatment planning and Quality Assurance (QA) at the BCCA, including the work described in this thesis.

2.3.3 Monte Carlo for Surface Dose Calculation

In contrast to most experimental methods, or many other dose calculation algorithms, MC does not rely on assumptions of equilibrium or fits to empirical function. As the behaviour of each particle is modelled directly, the absence of equilibrium between the transfer of Kerma and the deposition of dose arises naturally and is accounted for within the models. Likewise, particle transport across tissue inhomogeneities are modelled directly, and the properties of the local medium are considered, via sampling from appropriate probability distributions, at

each MC step. Therefore, inhomogeneity corrections are unnecessary. This makes MC is an ideal tool for investigating dose in the build-up region or in bolus-surface air gaps.

In fact, very little literature appears to question the efficacy of MC simulations in addressing surface doses. Attempts to validate MC results in the build-up region, by comparison of calculated PDD with ionization chamber measurements, showed excellent agreement to experimental values for 6 MV beams[5]. At 18 MV, some small discrepancies between simulation and experiment were observed in several studies. The scale of the observed anomaly was in general very small, and was only of notable consequence in the build-up region where high-dose gradients can amplify the effects of small differences. After several possible causes for this behaviour were investigated, the general verdict within the literature is that the effect is not due to the MC simulations but rather due to error in how the chambers were represented within the simulations [28, 33].

The most common use of MC simulations within the literature concerning surface dose determination, appear to be for additional validation of experimental methods. Earlier in this Chapter we discussed how common dosimetry methods, specifically PP chambers and radiochromic film, tend to overestimate surface dose. Several studies have utilised MC simulations to provide an estimate of the "true" surface dose so that the scale of any overestimation or necessary corrections may be determined[9, 21, 37].

MC is not without its flaws. Given the large number of researchers working on extending and improving the application of MC simulations to radiotherapy, it would be quite unreasonable to expect that there is a single, unified method for performing these calculations. There are several competing programs to choose from, multiple different algorithms for treating certain aspects of particle behaviour, and a range of settings that define the "depth" and detail to which the particle histories are reproduced. Whenever a simulation is run, the user is given the opportunity to adjust various parameters and fine-tune the calculation to their

needs. Exploration of the literature reveals that the choice of these parameters can effect the results of the MC, particularly in the build-up region.

At a conference in 2009, Takeuchi et.al presented the effects of user-specified parameters on doses in the build-up region calculated with the EGS5 code [45]. The two parameters studied were the Electron Cut-off Energy (ECUT) and electron production cut-off energy (AE). The ECUT value specifies a lower bound for electron energy, below which an electrons history is terminated and the remaining energy is deposited locally within the medium. The value of AE specifies the minimum energy transfer necessary to trigger the production of a secondary electron. The choice of these values represent a trade-off between accuracy and computing time. Higher values will reduce the CPU cost by reducing the number of calculations that comprise an electron history, and reducing the number of electrons that must be calculated. However, a value that is too high can miss key events and reduce the accuracy of the model. Typical values for both ECUT and AE are 0.521 or 0.700 MeV[31, 38].

Takeuchi's results show that a choice of larger value thresholds (ECUT = AE = 0.700 MeV) can lead to significant underestimation of surface PDD compared to simulations using more accurate limits (ECUT = AE = 0.521 MeV). The difference in dose values reached as high as 14% for a 4 MV beam and a 30x30 cm^2 field. However, this discrepancy is significant only within a depth of 0.1 mm, and their work also show that a higher value, for either AE or ECUT, can result in a two-fold improvement in computing efficiency. Therefore, their recommendations are that the lower value limits are only necessary in special cases when accurate determination of surface doses are important (such as the current study).

Further work on this topic was published by Kim et.al in 2012[31]. This article is more relevant to our research as it utilises the same MC code, BEAMnrc and DOSXYZnrc, as our work. It is also a more extensive study that the work presented by Takeuchi et.al, as it also explored effects arising from the users choice of which algorithms are used to model

the transport of electrons. A Boundary Crossing Algorithm (BCA) is used to transfer the simulated electron across voxel boundaries within the virtual phantom. An Electron Stepping Algorithm (ESA) is used perform small deflections in an electrons path, simulating the multitude of small elastic collisions that will cause an electron to deviate from its line of motion. As with the values of threshold energies, the choice of which precise algorithm is used reflects a compromise between accuracy and efficiency. The reader is referred to the DOSXYZnrc documentation for further details on these algorithms and the options available [49].

Kim's results show that choice of electron transport threshold values and algorithms can result in differences of calculated surface doses as high as 10. In agreement with Takeuchi's results, Kim found that these effects are highly surface specific and that computational efficiency should only be sacrificed in cases where high accuracy in surface doses are required. In such cases, ECUT = AE = 0.521 MeV is recommended. With regards to the choice of ESA, either PRESTA-I or PRESTA-II, it was found that the former provided a significant improvement in computing speed but had little effect on calculated surface dose. In contrast, the choice of BCA was found to be more influential, and Kim recommends using the EXACT algorithm, as opposed to PRESTA-I, to yield more accurate results despite the loss of efficiency.

2.3.4 Comparison of Dose Calculation Algorithms Regarding Surface Dose

Previously in the chapter, we discussed the operating principles of the AAA algorithm as employed by the ECLIPSE^{TM} TPS. One of the strongest advantages of the AAA over some other dose-calculation methods is the use of MC simulations and experimental data to optimize mathematical models of the treatment beam in order to provide a more accurate recreation of a given treatment unit. The drawback to this method is that resulting calculations will be

biased by any methodological flaws in these simulations and experiments. As we have discussed, due to the high dose-gradient in the near-surface region, accurate dosimetry within the first mm of phantom depth can challenging. or For example, the necessary dosimetric data required to configure the AAA is most likely obtained using cylindrical ionization chambers which are unsuited to measuring accurate build-up dose. The issue of "effective point of measurement" can apply even to MC methods, where the results can depend on the size of the phantom voxels near the surface (this is a topic we will return to in Chapter 3).

The research evaluating the performance of AAA in calculating surface and skin doses is limited, and in most cases MC results are considered the "gold-standard" of comparison. Several of the relevant studies are primarily aimed at the study of tangental treatment fields such as commonly used in the treatment of breast cancer. A 2009 study by Panetierre et.al. compared AAA and MC results in the build-up region for a cylindrical phantom [36]. AAA was found to consistently underestimate near-surface dose (for 6 MV) beams over a range of beam angles between 15-75°. However, the authors dismissed the differences as clinically irrelevant, as the deviation is only significant for depths ¡ 1 mm, and even then are still within allowed tolerances. In contrast, similar work by Chakarova and colleagues found generally good agreement between AAA and MC for all depths, including the near-surface region [17].

Another study, by Chow et.al, considered treatment beams tangentially incident upon a cubic solid-water phantom. In this case, the central axis of the field was parallel to the surface plane of the phantom [20]. They calculated doses within a 2 mm thick slab at the phantom surface and found that AAA produced significantly higher values than MC, with the effects being generally worse for higher energies and small fields. Their final conclusion that AAA, and a related algorithm the Collapsed Cone Convolution method, cannot produce accurate dose predictions for depths $<$2mm.

More recent interest in the application of Stereotactic Body Radiotherapy (SBRT) has led to further review of the accuracy of dose calculations due to the small fields and high-dose fractions used in the procedure. In a conference proceeding from 2014, Cho et.al. compared skin dose values predicted using the AAA with MC and experimental measurements performed with EBT2 films and an Attix PP chamber [19]. Although MC results were found to be up to 3.5% higher than Attix measurements, skin dose values calculated with AAA were found to overestimate the experimental data by a much higher degree. For a 6 MV 10x10 cm^2 field, AAA predicted surface PDD to be 40% compared to a chamber value of 16%.

A tendency for AAA to *under*estimate surface dose was also observed by Walters et.al in an investigation of SBRT treatments applied to canine limbs [50]. An interesting aspect of this report is that the degree of deviation, between experimental and AAA results, was observed to be dependent on the dimensions of voxels used in the dose calculations, with smaller voxels found to be more accurate.

A key point that we have emphasised throughout this chapter is that accurate determination of dose in the near-surface region is a persistent challenge in dosimetry. The presence of non-equilibrium conditions and a high dose-gradient makes obtaining consistent and unambiguous results difficult. As we have seen, the issue of "point of measurement" is a recurring problem the effects both experimental and computerized methods. Given the rapid build-up of in the first few milimetres from the surface, measurements using different instruments, e.g. PP ionization chambers and radiochromic films, are effectively taken at different depths and so can have significantly different results. Computer simulations using voxels of different sizes is analogous to this situation with similar results. Using multiple techniques in an experiment, so that the results can be cross-validated, is an almost ubiquitous practise in dosimetry. However, this approach is much more challenging when the doses of interest are at the surface. We attempt to address this concern in the current investigation by normaliz-

ing each measurement using a suitable reference value obtained using the same method, and therefore we consider the relative effects of increasing bolus-skin distances. We will now discuss our methods in detail in the following chapter.

Chapter 3

Validation of Monte Carlo Methods

3.1 Introduction

Many modern radiotherapy techniques such as, IMRT, VMAT, and others, rely on *inverse planning*. To create a suitable treatment plan using this method, accurate computerised dose calculations are critical. These calculations must account for the many compounding variables present in the treatment room, including the application of bolus and the effects of any gaps between the bolus and the patient's skin.

Many commercial Treatment Planning System (TPS)s, such as ECLIPSE^{TM}, use convolution/-superposition algorithms to calculate dose. As described in Chapter 2, these programs use density-based rescaling to account for heterogeneities in the medium, presumably, including air gaps[20, 43]. Conversely, MC methods directly simulate the behaviour of "virtual" photons and electrons, determining the occurrence of interactions and energy transfer events using probability distributions based upon well-established physics. MC is widely considered the more accurate technique but comes at a higher computational cost, and so is less

widely available [7, 38]. The comparison of these algorithms' ability to accurately simulate the effects of bolus-skin gaps, is a central question in this thesis.

The work in this thesis also aims to lay the foundations for future exploration into both the essential physics and the clinical relevance of any gap effect. If effective, these simulations will also form the basis for a "virtual laboratory". In this space, individual parameters such as angle of incidence, beam shape, Multi-leaf collimator (MLC) collimation, and bolus shapes can be individually isolated and studied in an idealized environment. After exploring this wide parameter space, these findings can be applied to clinical situations for planning and quality assurance.

However, any computational tool is only useful if it can be shown to accurately simulate the physics of the scenario. Before we can use these techniques to explore the unique circumstance of bolus air gaps, it is necessary to confirm their results in a more standard situation.

In this Chapter, we will discuss our methods of validating our simulations by comparing calculated PDD curves, from both MC and Eclipse, with experimental data obtained with Gafchromic film and a Markus ® parallel-plate ionization chamber (manufactured by CNMC+, USA). For these studies, we used an open 6 MV beam, incident on a cubic water-equivalent phantom. This set-up was chosen for several reasons: Firstly, measuring PDD curves in these conditions is a standard test performed during the commissioning and quality assurance of a clinical linac[8]. Secondly, this method has been used several times in the literature as a means of validating simulations[16, 20, 38]. Thirdly, the virtual phantoms used for this process could be easily adapted to the study of air gap effects by the addition of a floating slab of water to serve as the bolus.

3.2 The Design of Virtual Phantoms

In our simulations we have taken the clinical context of a radiotherapy treatment requiring bolus, where a gap is present between the bolus and the patient's skin, and have simplified it to the most idealized scenario, as follows: A cube of water is irradiated by an open, 6 MV beam at normal incidence with a uniform slab of water serving as a bolus. The surface of the cubic phantom is positioned at 100 cm distance from the radiation source (an Source-Surface Distance (SSD) set-up) and the bolus is placed above. Air gaps are introduced by "floating" the slab above the phantom at fixed distances.

This general set-up is illustrated in Figure 3.1, below. The arrangement is essentially a virtual replica of the experiment performed by Khan et.al[30] to study bolus effects, which was adopted to provide an established point of reference within the literature.

The key element in this model is the construction of the phantom. DOSXYZnrc, the MC program used for this study, allows the creation of very simple phantoms [49]. Essentially, the user defines the outer limits of a cubic volume in a Cartesian space. This space is divided into voxels by entering the coordinates of each voxel's boundaries. Once the space has been voxelised, the users then "fills" the volume with a material of their choice, i.e. the voxels' mass-density is set to the value corresponding to the chosen substance, which is then used to calculate the transport of photons and electrons through that voxel. Materials can be assigned to individual voxels or to entire regions within the subject volume. The results are stored as a 3D density matrix in an **.egsphant** file.

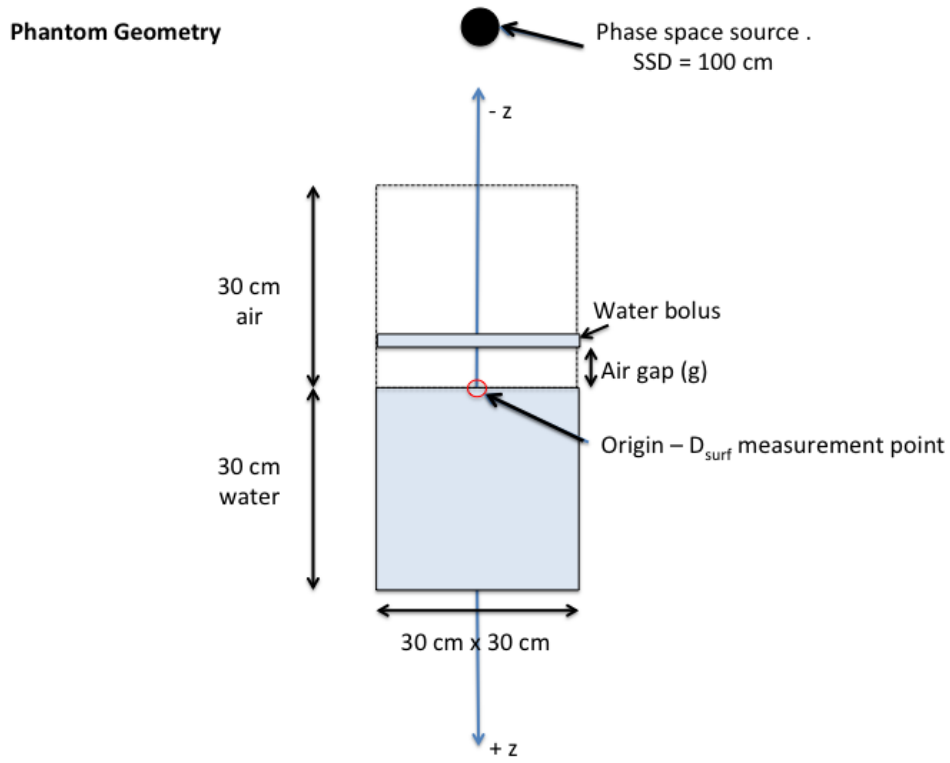

Figure 3.1: Schematic showing the apparatus used for our Monte Carlo simulations. The phase space source corresponds to the source of the virtual 6 MV linac. Note, that the origin of the system is defined at the centre of the phantom's surface. The bolus floats in air above the phantom within the negative -z region. Our measurement points are within the phantom body i.e. the +z region. Surface dose is measured at D_{surf}, which is located in the centre of the voxels immediately below the origin.

The virtual phantoms used for our simulations were created using this method, as it was believed to be the best way to create a truly "ideal" phantom. Other methods, such as creating a phantom from a CT renderings of a cubic phantom and a bolus, or by "drawing" the system in Eclipse, were either untested or might introduce sources of error such as slight angles in the positioning of the bolus or non-flat surfaces. By making our phantoms in DOSXYZnrc, we could ensure that our bolus was perfectly flat and of uniform thickness and density, allowing us to isolate the effects of bolus-surface gap sizes and field sizes alone.

For the purposes of our investigation, a suitable phantom should demonstrate the following criteria:

1. Simple geometry that can be easily adjusted and allows for a large range of bolus-skin distances.
2. Wide enough to allow multiple field sizes to be applied to the same phantom.
3. Deep enough the avoid complications to the backscatter in the near-surface region.
4. Water-equivalent.
5. Can be introduced into Eclipse for treatment planning and AAA dose calculations.
6. Total number of voxels in the phantom should be small enough to allow for reasonable computation times.
7. Simulations should deliver accurate PDD values in the very near surface region.

As shown in Figure 3.1, our model is constructed from a 30x30x60 cm^3 volume. The upper region (in the -z range) is filled with air, whereas the lower region (+z range) is made of water and defines the actual "body" of the phantom. A bolus was constructed by converting a slab of voxels in the upper half, spanning the whole xy plane and with a depth corresponding to 1 cm, into water. By reducing the upper and lower z boundaries of this slab, the bolus is effectively "floated" up from the phantom surface to provide a set range of air gap sizes (g). A new .egsphant file was created for each bolus-skin value studied. If no bolus is present, as in the validation experiments described in this chapter, the entire upper half of the system remains as air.

Finding an appropriate choice of dimensions for the voxels required some trial and error. This is due to the conflicting demands of items 6 and 7 in the above list. To limit the number of voxels and maintain a reasonable CPU time in a phantom of this size, those voxels need

to be quite large. However, if the voxels are too large the calculated surface dose becomes less accurate. As discussed in Chapter 1, high-dose gradients are present near to the surface due to the lack of electronic equilibrium in the build-up region. With large voxels, these gradients are averaged out leading to an overestimation of dose. This is analogous to the issues presented in experimentally measuring accurate surface doses using large-cavity ionization chambers.

Our original design used uniform voxels of 0.25x0.25x0.25 cm^3. Monte Carlo simulations of a 10x10 cm^2 field incident on this phantom calculated the PDD at the D_{surf} point aas $43 \pm 2\%$. This is high compared values obtained in the literature, which are typically 14-16%, depending on the exact study and measurement method used [12, 21, 25, 37]. It should be noted that with the given voxel size, the depth of the D_{surf} point is 0.125 cm, which is substantially deeper than the standard reference depth for "skin" dose (70 μm). The results of our simulations are consistent with available values for the similar depth of 1 mm[12, 21], indicating our simulations are accurate but also that this voxel size is insufficient for the the study of surface dose.

To achieve accurate surface dose whilst limiting the number of voxels, we decided to use a phantom composed of two different "grades" of voxel size, shown in Figure 3.2. In the near-surface region, where more fine-grained measurements are required, we use voxels of 0.25x0.25x0.005 cm^3. After a depth of 1 cm, the voxels are restored to the more standard 0.25x0.25x0.25 cm^3. Using this format, the measurement depth of the first voxel layer is 25 μm, which corresponds to the measurement depth of the Markus PP chamber (0.0025 g/cm^2)[2] and the second layer is 75μm, which is a good match to the standard for skin depth. At the second layer depth, calculated surface PDD was $19.2 \pm 0.14\%$, which is much closer to the values found in the literature.

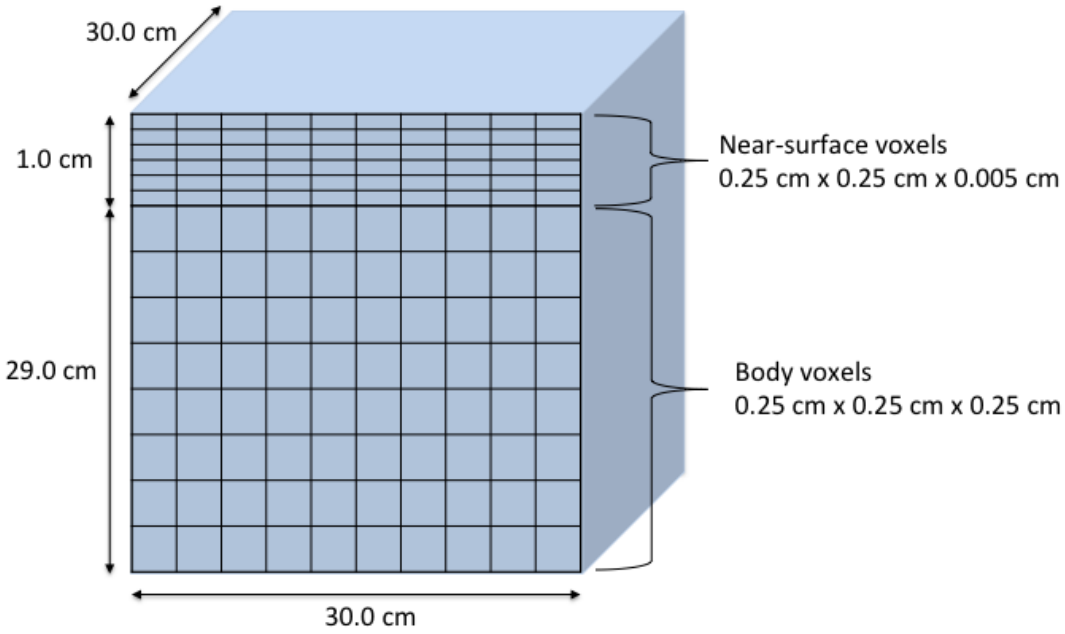

Figure 3.2: Schematic showing the voxel distribution for the virtual phantom used in our MC simulations.

The use of two different voxel sizes did introduce concerns as to whether results from the two voxel grades would be comparable, and if the results could be used to construct a single PDD curve for the whole phantom without introducing artifacts. This issue was addressed by comparison to experimental PDD data as part of the validation experiments we discuss later in this chapter.

However, as discussed in the next section, the use of this 2-voxel phantom did introduce some further complications when it was found to be incompatible with the use of the Eclipse TPS.

3.3 Interfacing DOSXYZnrc and Eclipse

For several years, the BC Cancer Agency (BCCA) has utilized an automated process that allows MC absolute dose calculations of clinical treatment plans using actual patient data. The program takes treatment plans created in ECLIPSE^{TM} and converts them to input files for DOSXYZnrc and BEAMnrc so that a MC simulation of the plan can be performed. In addition, the CT data, used to define PTV and at-risk structures in treatment plans, can converted to an .egsphant file, creating a virtual phantom of each individual patient.

This system was developed in-house as a QA method, with contributions from numerous staff and students at the BCCA, notably Tony Popescu [38], Tony Teke, Alanah Bergman [11] and Parmveer Atwal. The whole program is comprised of many subprocesses, each with its own function and methodology, e.g. the particular MC algorithms and error-reduction methods used, the derivation of coordinate transformsations between ECLIPSE^{TM} and DOSXYZnrc "spaces", implementation of MLC beam-shaping, and a great deal more. The discussion of these aspects are far beyond the purview of this thesis and so we will focus our attention on the particular modifications developed for this investigation.

One of the key issues addressed in this investigation was to compare the ability of AAA and MC to accurately simulate the effects of bolus-skin gaps on surface dose. For this purpose, the use of the BCCA's interface between ECLIPSE^{TM} and DOSXYZnrc was an excellent tool. The simple open-beam set-up described above could entered into Eclipse as a treatment plan and the dose distribution would be predicted using AAA. The QA script would then be used to export the treatment plan for MC dose calculations and the results compared.

However, although the existing QA scripts include methods for converting patient CT data into .egsphant files, no process existed to import existing .egsphant files into ECLIPSE^{TM}. Therefore, we developed a script in MATLAB to convert our idealized bolus phantoms into

a format that could be introduced into the TPS. The key task of this script is to extract each plane of an .egsphant phantom and convert it to a CT image slice stored in a **DICOM** file. The full set of images can be imported into ECLIPSE^{TM} and combined into a 3D model, recreating the original phantom.

Unfortunately, as mentioned in the last section, the different voxel dimensions within our phantom proved to be incompatible with conversion to a 3D "pseudo-CT" rendering. When constructing a 3D representation of the subject, ECLIPSE^{TM} (and most medical imaging software) assumes that the image slices are all of equal thickness. Our phantoms have both 0.005 cm and 0.25 cm slices along the z axis. The software assumes 0.25x0.25x0.25 cm^3 voxels and so the resulting phantom appears to be stretched out in the z direction. Attempts to compensate or correct for this effect have proved unsatisfactory.

A compromise was accepted where phantoms of uniform, 0.25x0.25x0.25 cm^3 voxels were used to create the original treatment plans, and for AAA dose calculations. However, after converting the plan into a DOSXYZnrc input file, the "fine-grade" phantom was used for MC calculations.

Despite the use of two phantom variants, it was not believed that this would affect the plan or the dose calculation. Although energy is deposited into a medium by the actions of subatomic particles, dose is a macroscopic property. The phantoms may differ in voxel resolution but they still represent identical bodies, composed of the same material and of the same size, being subjected to the same treatment under the same conditions. The subject of the investigation has not changed but the scale of measurement is different. Our interest in bolus confirmation primarily relates to *skin* dose, where the relevant depths are between 50-100 μm. The thin voxels used in our MC phantom reflects a choice of measurement tool more suited to this scale.

Our approach to addressing this issue had two parts: Firstly, we analysed results over a wide-range of depths so that corresponding data points can be compared. This was achieved by the comparison of MC and AAA PDD curves as part of the MC validation described in this chapter. Secondly, we concentrated our analysis regarding the treatment of bolus air gaps, on the discussion of *relative* effects rather than direct comparison of absolute dose values. This will be elaborated upon further in Chapter 4.

3.4 Monte Carlo Simulations and Analysis.

In laying the groundwork for MC study of the bolus gap effect, our simulations have focused on the influence of two key parameters, the distance between the bolus slab and the surface of the body, and the field size of the treatment beam. These factors were chosen as the literature demonstrates that both variables have an effect on surface dose in the presence of an air gap [13, 30, 44].

Virtual phantoms were to represent the following bolus configurations:

- No bolus present
- Bolus in full contact with the phantom ($g = 0$)
- Bolus with gap sizes of $g = 0.5$, 1.0, 2.0, 3.0, 4.0, 5.0, 10.0, 15.0, 20.0 cm.

Four variants of the same open-beam treatment plan were created for each of these phantoms using a square field of size 5, 10, 15 or 20 cm. Therefore, a total of 44 separate plans were created in Eclipse and 44 AAA and MC dose calculations were performed. The flow-chart in Figure 3.3 depicts the key steps used in planning and running each one of these plans in DOSXYZnrc and ECLIPSE^{TM}.

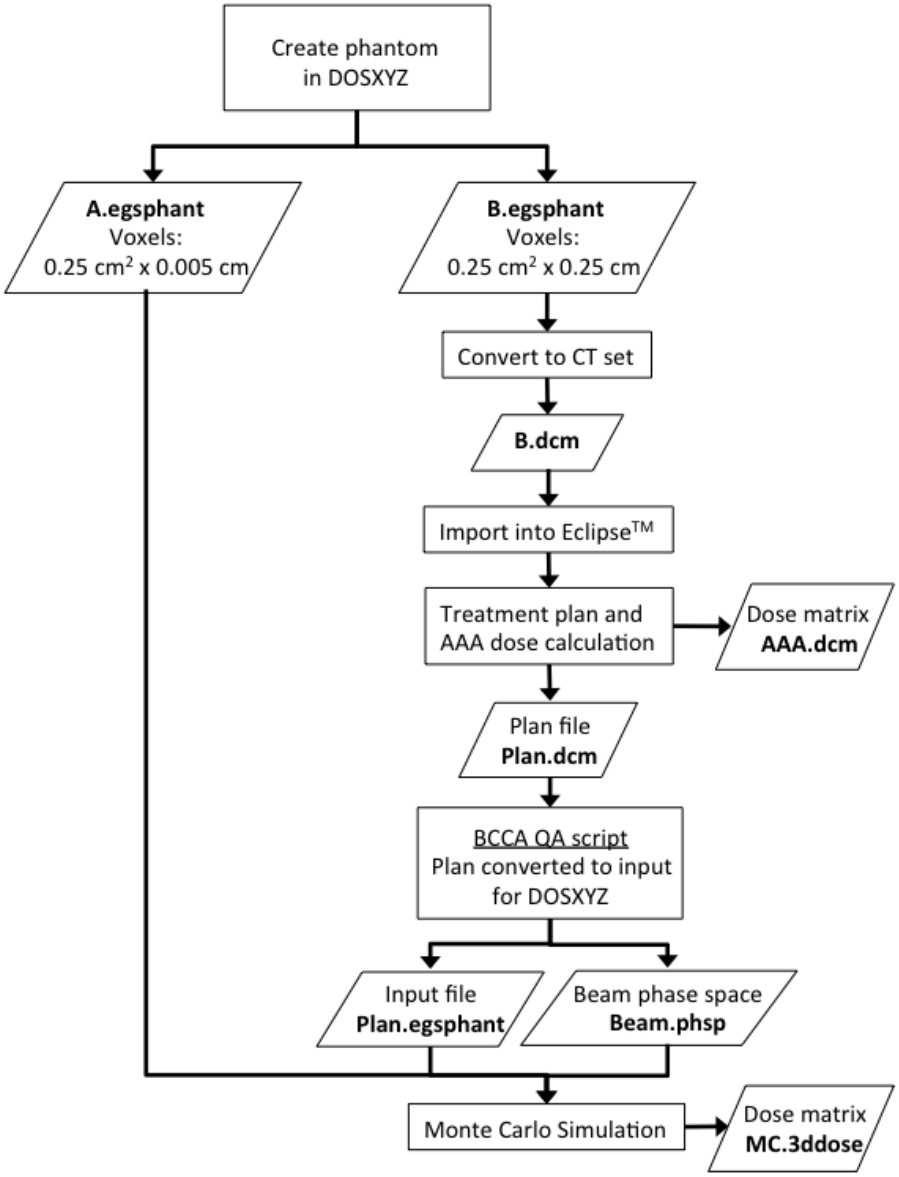

Figure 3.3: Flow chart illustrating the process used to create MC simulations from ECLIPSE™ treatment plans using idealized virtual phantoms. Rectangular boxes represent processes and parallelograms indicate output files that would be fed into other subsequent steps.

In all cases, the treatment was to deliver a prescribed dose of 100 cGy to a point located at the centre of the phantom surface (the D_{surf} point shown in Figure 3.1). The PTV was defined to include the entire 30 cm^3 volume of the phantom's "body". The simulated linac used for both treatment planning and MC calculations was a Varian Clinac iX and the central axis of the 6 MV beam was incident directly through the bolus, i.e. along the z-axis defined in Figure 3.1.

The QA script employed by the BCCA sets the parameters for the Monte Carlo algorithm when converting a treatment plan into a DOSXYZnrc input. In using this script to set-up our simulations we have adopted these values with little modification. The most relevant values used in our DOSXYZnrc simulations were:

- Number of simulated particles was N = $5x10^9$
- Global photon and electron transport cut-off were PCUT = 0.01 MeV and ECUT = 0.7 MeV
- Threshold for the production of Bremstrahlung photons was AP = 0.01 MeV
- Threshold for the production of knock-on electrons was AE = 0.7 MeV

The MC calculated dose for each voxel in the .egsphant phantom forms a dose matrix, which is recorded as a **.3ddose** file. The QA script automatically performs 3D Savitzky-Golay filter on this dose matrix to reduce the effects of stochastic noise in the results [27]. This is an example of a *Variance Reduction Technique*, such as commonly employed in Monte Carlo studies and full details of this filter can be found here [11]. The script also creates a new .3ddose file containing absolute dose values (in Gy), which are determined by multiplying the filtered dose matrix by a scalar conversion factor[38].

Once the AAA dose calculations and 7MC simulations were performed, the results were analysed in MATLAB. Simple scripts were developed to extract and plot key information such as PDD curves, lateral dose profiles and surface dose. These scripts are given in the appendix.

3.5 Experimental Validation of Simulated PDD Curves

It had been stated previously that computerised dose calculations are a useful tool only if they can accurately predict and reproduce results obtained through direct, physical measurement. To confirm the validity of our MC methods, and to assess the possible effects due to the modifications discussed above, we have compared simulated PDD curves with measurements obtained using both a Markus parallel plate ionization chamber and EBT3 Gafchromic films.

With regards to surface dose measurements, most sources consider extrapolation ionization chambers to be the most accurate and reliable method[21, 25]. However, in the absence of such an instrument parallel plate chambers have been shown to produce accurate results provided a suitable correction factor is applied[25]. Therefore, we selected a parallel plate ionization chamber as our primary tool for our validation study and later measurements of surface dose.

Radiochromic films are widely considered a less reliable dosimetry tool [23], due to issues concerning variability between film sheets and a strong dependence on processing and analysis methods. However, unlike ionization chambers that can only report dose at a single point, films can be used to measure the distribution of dose across a plane. This ability was considered particularly relevant for later experiments concerning the effect of bolus-skin gaps on lateral surface dose profiles, and so, EBT3 films were also used during our validation measurements.

The diagrams below illustrate the apparatus used for PDD measurements, with PP chamber and EBT3 films. A 6 MV Varian Clinac iX was used to irradiate the phantoms with a total dose of 100 MU, delivered at a rate of 600 MU/min, using square fields of 5, 10, and 15 cm.

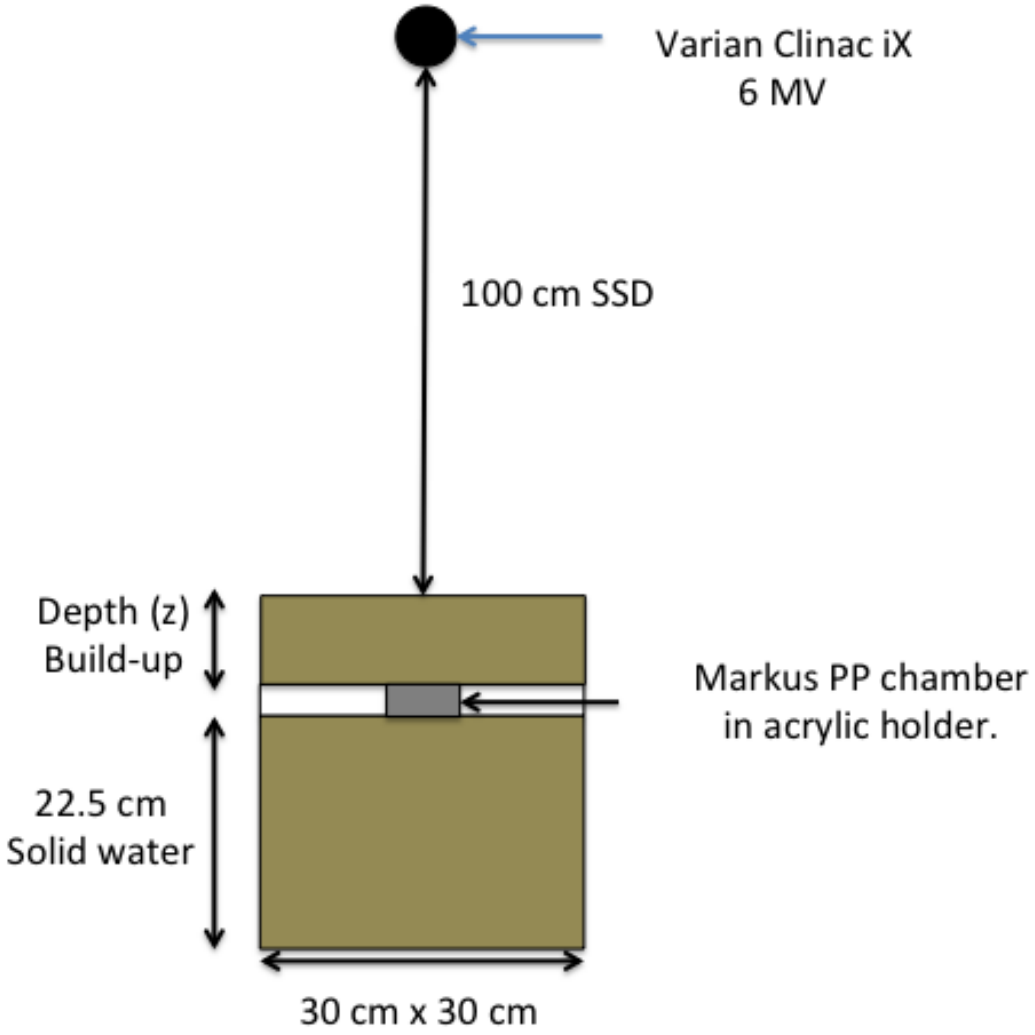

Figure 3.4: The experimental geometry for PDD measurements with a Markus parallel-plate ionization chamber

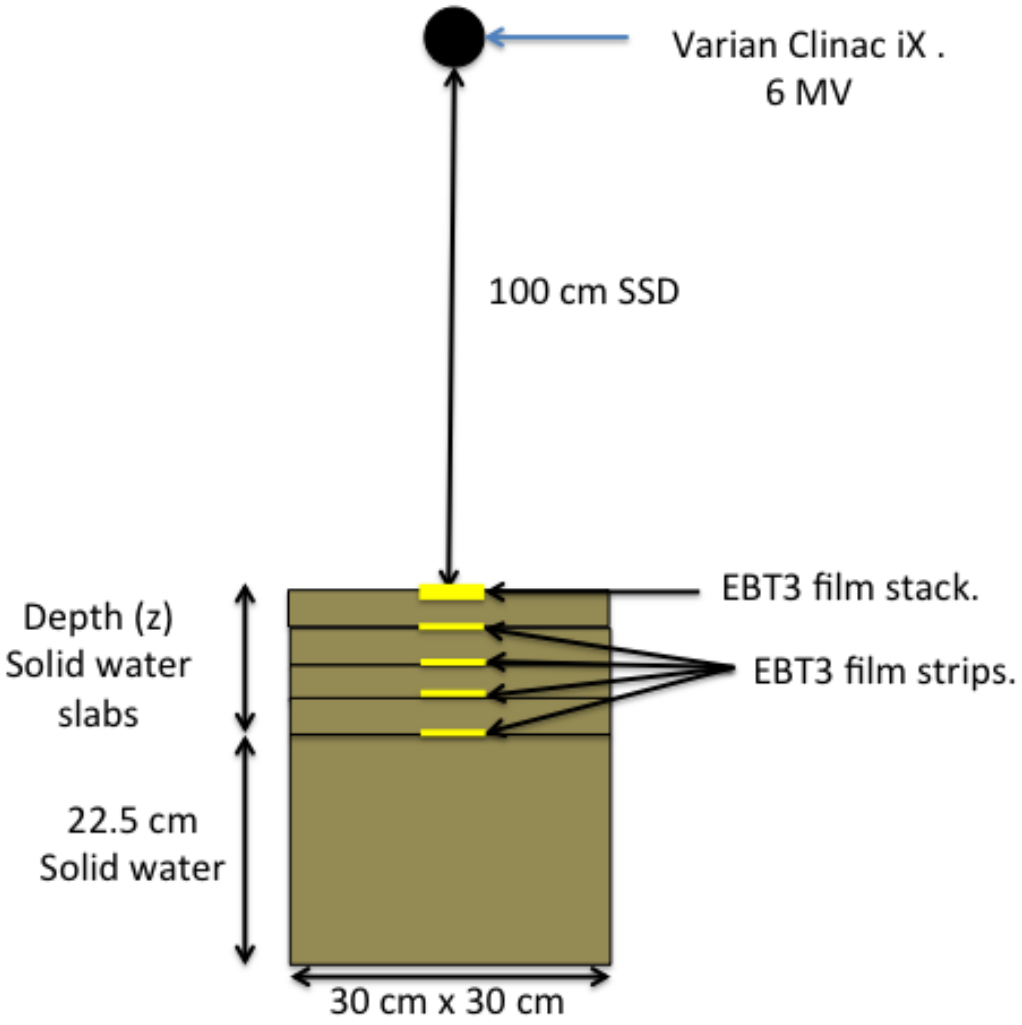

Figure 3.5: The experimental geometry for PDD measurements with EBT3 radiochromic films.

PDD measurements were conducted in a solid-water phantom, with the exception of a 1 cm thick slab of acrylic which was used to hold and surround the Markus chamber. In the absence of additional build-up material the point of measurement was taken to be the inner surface of the chamber entrance window, at a depth of 0.0025 g/cm^2[2]. Measurement depths between 2 mm to 16 cm were obtained by placing layers of solid water upon the

chamber, and adjusting the couch height to maintain a SSD of 100 cm. The solid-water sheets available were too thick to conduct measurements at depths $z < 2$ mm, therefore, sheets of EBT3 films (from an expired batch) were used to provide the necessary build-up at this range. The effective thickness of a single EBT3 film was estimated to be 0.0378 g/cm^2, based on information from the manufacturer's user guide[3]. Therefore, for example, placing two sheets of film over the Markus chamber results in an effective measurement depth of 2 $\times$ 0.0378 g/cm^2 + 0.0025 g/cm^2 = 0.0781g/cm^2.

The charge $Q(z)$ within the chamber cavity was measured with an electrometer. For each depth point (z), three charge values were measured for both +300 V and -300 V. The mean absolute magnitude of all six electrometer measurements, was used as the final value of charge accumulated. The standard error was used as a measure of the stochastic error in the charge value, which was combined with an estimated electrometer error of 0.01 C, using standard methods. The average relative uncertainty in the charge measurements was less than 0.3 %.

Each experiment run, for both instruments and all field sizes, included a measurement at 1.5 cm depth - the standard value of z_m for 6 MV beams. The charge collected at this depth was assumed to be the maximum charge, and PDD was calculated as the ratio:

$$P'(z) = \frac{Q(z)}{Q(z_m)} \times 100\% \tag{3.1}$$

In Chapter 2, it was noted that PP chambers have been shown to overestimate PDD in the near-surface region and that this effect can be accounted for by the use of a correction factor. For our work we have utilised the correction derived by Gerbi and Khan, where the corrected PDD $P'(z)$ can be calculated from the raw data $P(z)$ using Equation 3.1[6, 25].

$$P'(z) = P(z) - \varepsilon(0) d \exp\left(-\alpha \frac{z}{z_m}\right) \tag{3.2}$$

In this expression d represents the separation between the parallel plates of the chamber, which was 2 mm for the Markus chamber[2]. α is an empirical constant determined, by Gerbi and Kahn, to be approximately equal to 5.5. $\varepsilon(0)$ represents the degree to which the chamber can be expected to overestimate the PDD at the surface and can be determined from the Ionization Ratio ($IR = 0.664$) of the linac and the distance between the sidewall and collection electrode ($C = 0.35$ mm) for the chamber used. Gerbi and Khan determined that their correction method typically provided PDD values within ≈ 1.3 % points of their extrapolation chamber results. This value was taken as an estimate of the systematic error of the correction process and, together with the value of the error in $P(z)$, indicated that the absolute uncertainty our corrected Markus PDD is less 1.4%.

$$\varepsilon(0) = (-1.666 + 1.982 \text{ IR}) \times (C - 15.8) \tag{3.3}$$

For film measurements, 2x3 cm^2 pieces of were cut from a single sheet of EBT3 film. Care was taken to ensure that the long axis of each piece coincided with the long axis of the original sheet to avoid artifacts that may be caused when comparing films of different orientations. Unlike ionization chamber measurements, where measurements at each depth must be performed individually, all films used to construct our PDD curves could be irradiated simultaneously, as shown in Figure 3.5. The edges of each film piece were firmly taped to the underlying solid-water to prevent air-gaps, which are known to affect the dosimetric accuracy of the film.

As with the Markus chamber, sheets of EBT3 were used as build-up material to allow measurements at depths under 2 mm. Inspired by the relevant work of Butson.et.al [12, 14], we

created a stack of four film pieces and placed it directly on top of the phantom with its centre along the central-beam axis. Using this approach, each film within the stack provided a value of $P(z)$ in the near-surface region of the PDD curve. The plane of measurement within each film was assumed to be at the centre of the active layer, at an effective depth of 0.0189 g/cm^2 within the film. Therefore, the depth of measurement for a given piece, within the stack, was 0.0189 g/cm^2 plus the total thickness of the film of the film layers on top. As with individual films, the edges of the stack were bound with masking tape to minimize air gaps.

The beam conditions for irradiation of the films were the same as those used for the Markus chamber measurements.

For use in dosimetry, the optical density of a batch of film must be calibrated by exposure of a sample sheet to known doses. The linacs in use at the Vancouver centre are calibrated to provide an output of 1 cGy/MU, delivered at z_{max} and using an SAD geometry. Therefore, the measurement plane was adjusted so that the films were at a distance of 100 cm from the source and 1.5 cm of solid-water build-up was placed on top. Three reference films were used, each being exposed to doses of 0, 80 or 200 cGy.

The EBT3 films were stored in opaque envelopes for a minimum of 24 hours before being digitized using a Epsom 10000 XL flatbed scanner. The long axis of the scanner was aligned perpendicular to the long axis of the film pieces. FilmQA Pro software (Advanced Materials, Ashland) was used to create dose maps from the scanned images. The conversion to dose is performed by identifying and selecting regions of interest on the reference films. The software determines the optical density in each of these regions and assigns the correct calibration dose in cGy. From these reference points, the software dose for each pixel of the image was determined by interpolation using a function fitted to dose-response curve determined for the film batch used. A suitable response curve was already present in the software at the time of our analysis and so additional calibration experiments were unnecessary. This

curve had been created by Joel Beaudry, a Physics Assistant at the BCCA Vancouver centre. The resulting dose maps were exported as **.tif** files and analysed in MATLAB.

The dose received by each film strip was determined by averaging the pixel values across a 10x10 pixel^2 region. These squares were centred at the midpoint of each film piece to avoid possible artifacts, such as scratches or stress cracks, that could be present at the cut edges of each piece. Before averaging the dose within each region, the influence of "spikes" were minimized by applying a 2D median filter. As with the Markus chamber measurements, doses measured at a depth of 1.5 cm were taken to be the maximum dose and used to determine the PDD for all other data point.

The standard error of the mean dose for each depth was typically less than 0.5 cGy. The systematic error due to the mapping of optical density to dose, as performed by FilmQA Pro, was estimated using the RMS difference between the mean dose of the reference films and their known dose values. This error was found to be $\approx$ 0.9 cGy. When combined and propagated using standard methods, this resulted in typical absolute uncertainties in the PDD values of $\approx$ 2.0%.

3.6 Results of the Validation Experiments

Figure 3.6 shows simultaneous plots of PDD curves obtained using MC, ECLIPSE^{TM}, EBT3 Gafchromic films and a Markus parallel-plate ionization chamber for all three field sizes studied. These results depict the distribution of dose along the central-beam axis in the absence of any bolus material. It can be readily seen from these curves that our MC simulations display excellent agreement with experimental measurements. This is especially prominent for the comparison between the Markus chamber and the MC data. Film data also shows good general agreement with the simulations, however, some data points are clear outliers. Although care was taken to account for systematic effects known to effect the dose response

of films, such as their orientation or their scan direction [23], the behaviour of some film pieces could still have been perturbed. One possible cause of this could have been the presence of an air gap between the film and the solid water medium, despite the use of tape to try and assure full contact.

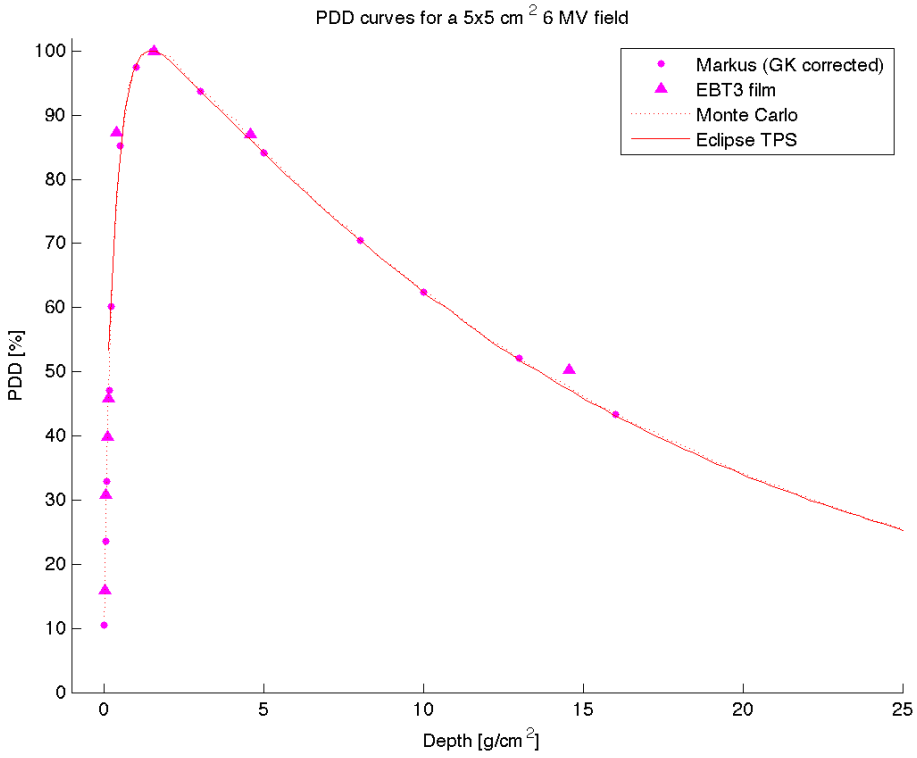

(a) 5x5 cm^2

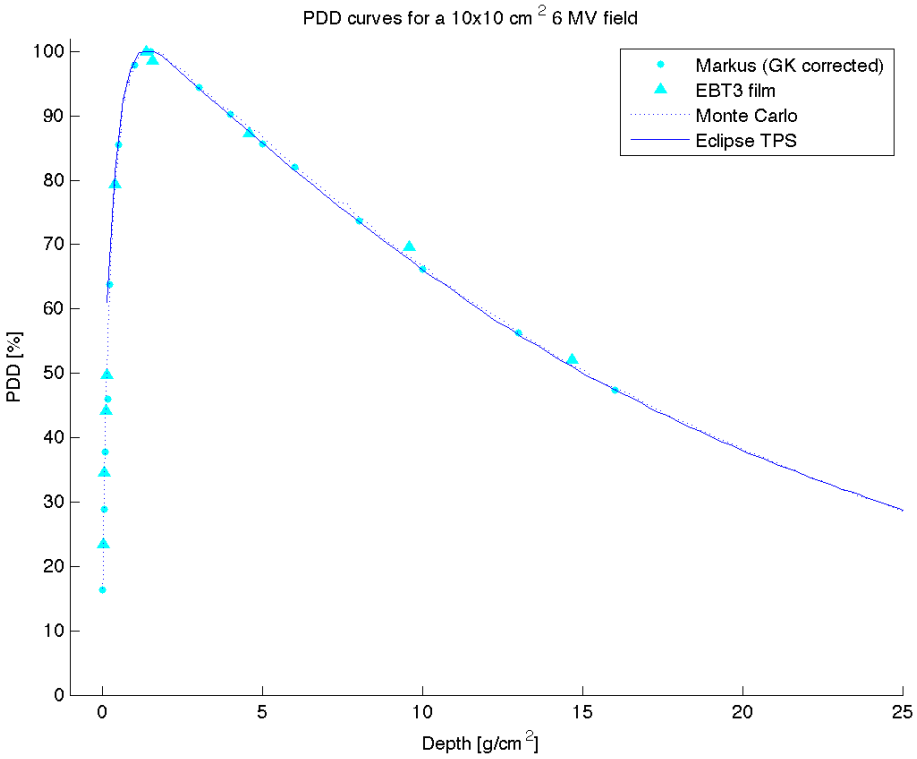

(b) 5x5 cm^2

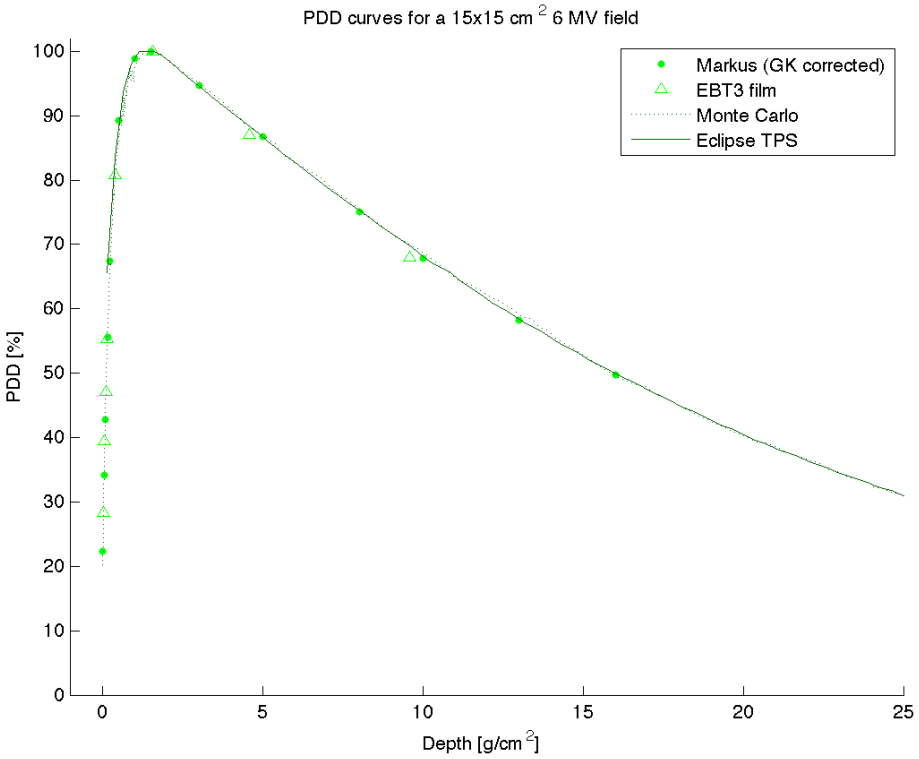

(c) 5x5 cm^2

Figure 3.6: Comparison of PDD curves, obtained using a Markus parallel plate chamber, EBT3 films, MC, andAAA for 5x5, 10x10 and 15x15 cm^2

To allow for a more thorough discussion of the results, Figure 3.7, shows the build-up regions of the PDD curves depicted above. At this scale, the most notable feature is the divergence between AAA results with experimental and MC data in the near-surface region. The AAA results can be seen to significantly overestimate the PDD, relative to MC, in the first voxel. The difference between AAA results at 0.125 cm and MC results, at the comparable depth of 0.1225 cm, was 8.3%, 11.7%, and 13.5%, for 5,10 and 15 cm^2 fields, respectively.

There are several possible reasons for this discrepancy. The first is that the phantoms used for the ECLIPSE^{TM} calculations possessed larger surface voxels than those used for MC calculations, and so the larger dose gradient in the build-up region would have been averaged over a greater depth. However, MC calculations performed with the larger (0.25 cm^3) voxels yield a surface PDD of $\approx 47\%$ at 0.125 cm depth with a 10x10 cm^2 field, which is consistent with literature results of 43% for 1 mm[21] but still lower than the AAA predictions of 61%.

Another reason for ECLIPSE^{TM}'s overestimation of surface dose, is that the beam model used by the AAA algorithm is dependent upon empirical corrections based upon clinical beam data, typically acquired during commissioning and calibration of the machine[43]. Therefore, the results of the algorithm are, to some degree, contingent upon the accuracy of these measurements. Using an ionization chamber that is unsuited to surface dose measurements, such as a Farmer chamber, or if corrections such as the Gerbi-Khan method are not applied, could lead to a systematic overestimate of dose that is specific to the surface. This is illustrated by comparing our MC and ECLIPSE^{TM} results with QA data acquired using a raster scanned ionization chamber (a IC 10 Wellhofer thimble chamber) in a water tank (Figure 3.7(d)). This data was provided by Vancouver Physics Assistant, Vince Strgar. The AAA results show fair agreement, which adds weight to our premise that the entered beam data could result in an overestimate of surface PDD.

In general, the results of our MC calculations show excellent agreement with experimental data, despite the modifications we have made to the standard simulation process. The MC simulations accurately mimic the physical behaviour of a 6 MV beam incident on a water-equivalent cube and so can be considered valid for further use in the study of bolus air gaps.

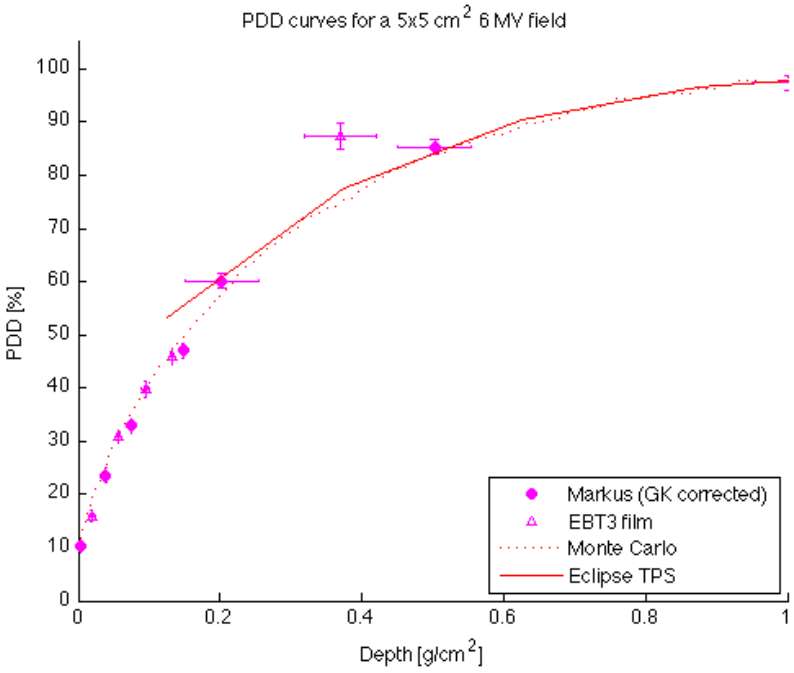

(a) 5x5 cm^2

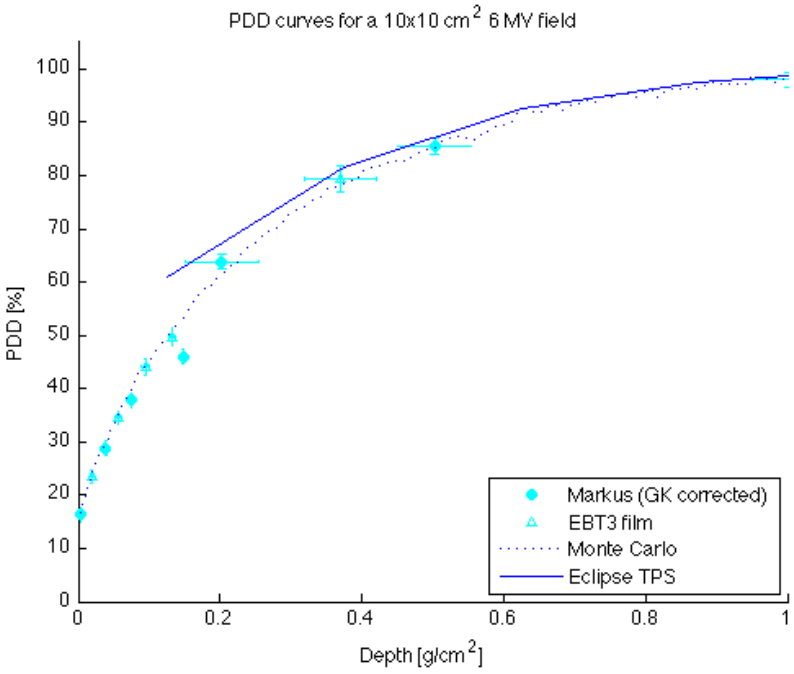

(b) 10x10 cm^2

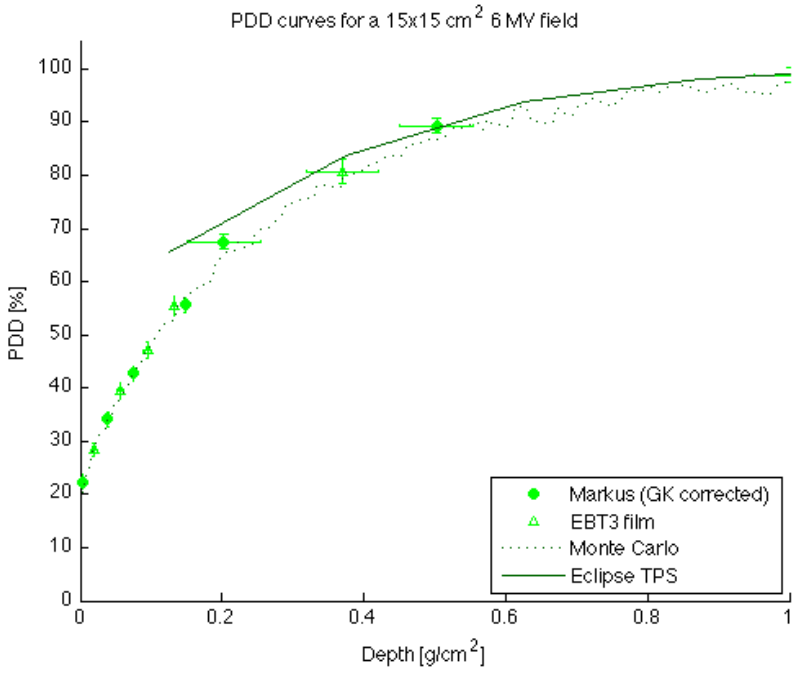

(c) 15x15 cm^2

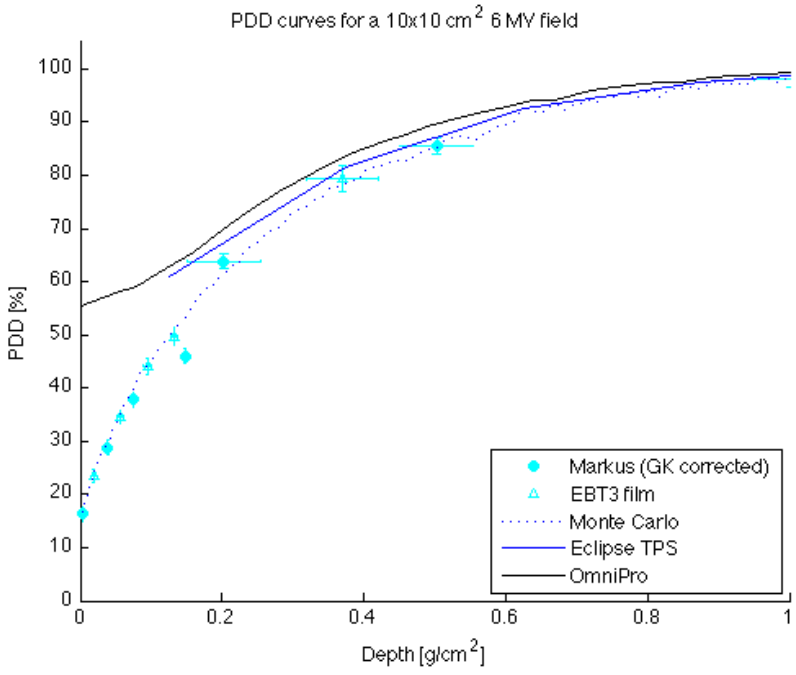

(d) 10x10 cm^2 with OmniPro data

Figure 3.7: Comparison of the build-up region for PDD curves, obtained using a Markus parallel plate chamber, EBT3 films, MC, and AAA for all field sizes.

Chapter 4

The Effects of Bolus-Skin Gaps on Surface Dose

4.1 Introduction

Accurate and efficient dose calculation underpins all aspects of radiation treatment, from ensuring patient safety to QA. High-precision dose-sculpting methods, such as VMAT, require high-quality dose calculations to create the treatment plan itself. However, with greater precision in the control of dose distribution comes increasing standards for the accuracy of dose calculation. To reduce the occurrence of skin toxicity in patients, accurate prediction of surface dose is necessary. This includes the ability to simulate and reproduce the effects of possible perturbing factors, such as the presence of gaps between a bolus and the patient's skin.

To investigate the effects of these gaps on surface dose, and the effectiveness of MC and AAA calculations in reproducing these effects, we have conducted a study inspired by the work of Khan[30] described in Chapter 1. Our "virtual" treatments are a computer reproduction

of this study, and we confirm the results of these simulations using ionization chamber and EBT3 film measurements.

4.2 Measuring and Analysing Surface Dose Effects

For constructing and running the simulations, the same process as described in Chapter 3.3 was used. However, for this study the phantom files also included a 1cm thick bolus of water that was "floated" at set distances above the main body of the phantom. Otherwise, the beam energy, field sizes, SSD and angle of incidence were the same as described for the validation study.

The apparati used for ionization chamber and film measurements are shown in Figure 4.1. As with the computerized methods, the core elements of the arrangement are the same as was used for measuring the PDD curves, described in Chapter 3. However, for the specific purposes of this study, the only point of measurement was at the surface of the solid-water phantom. A 30x30x1 cm^3 slab of solid-water was introduced to serve as our bolus. The slab was supported by four spacer posts with adjustable heights to create well-defined gaps between the bolus and the phantom. These posts were constructed from interlocking bricks made from a thermoplastic material (acrylonitrile butadiene styrene) i.e. LEGO^{TM}. To try to approximate the gap sizes g used in the computer simulations, various combinations of three different types of bricks were used:

- A "standard" brick. Height = 1.149 cm.
- A base brick. Height = 0.502 cm.
- A flat brick, similar to the base bricks but with no 'bumps. Height = 0.313 cm.

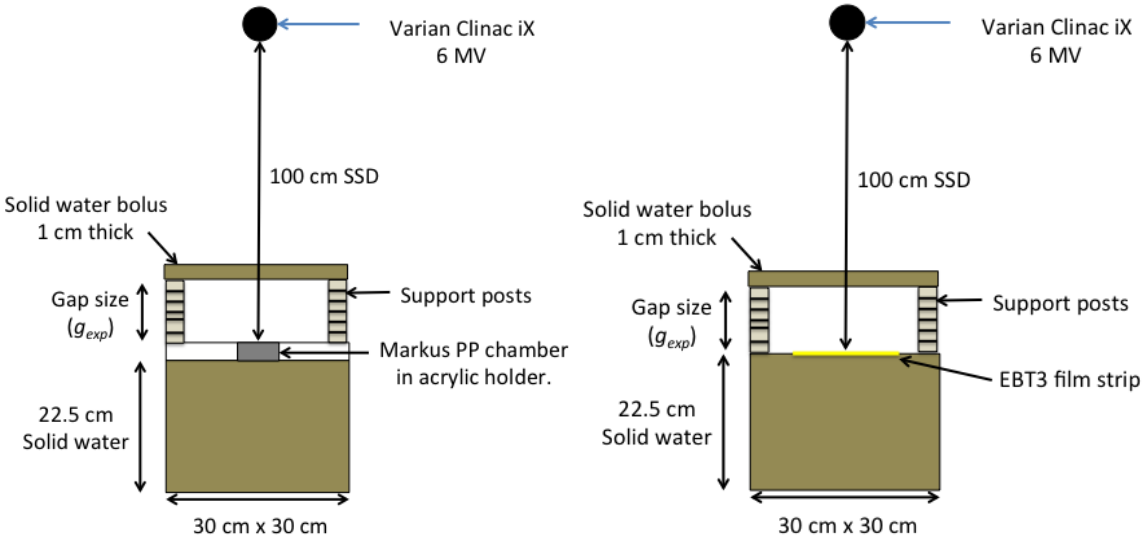

(c)

Figure 4.1: Experimental procedure for measurement of surface dose with increasing gap size, using a Markus parallel plate chamber (a) and EBT3 film (b). c) A photograph showing the phantom and bolus assembled for use in Markus chamber experiments.

These brick heights reported above were measured using a micrometer screw gauge. Repeated measurements of the same brick, and of different bricks of the same type, resulted in the same value. This would indicate that the statistical variance between these bricks is smaller than the precision of the micrometer $\pm$ 0.001 cm. All support posts were constructed from these bricks in the same manner for a given height, yielding experimental gap values in the range of 0.5 to 5.3 cm. The gap sizes were confirmed at each stage of the experiment by directly measuring the distance between the surface of the phantom and the bottom surface of the bolus slab, at the centre of all four sides of the phantom, using a micrometer. We also digitally measured the surface incline of the solid-water bolus with respect to phantom surface and the treatment couch. The measured incline was consistently below 0.1°. Based on these results we, conservatively, estimate the uncertainty in g_{exp} to be $\approx$ 0.005 cm.

It is important to note that long strips of EBT3 films (2x20 cm^2) were used for surface dose measurements, unlike the small pieces that were used to construct the PDD curves shown in the preceding chapter. The long axis of these strips were oriented along the x-axis of the beam, using the markings of the linac's light field as a reference. Longer strips were used so that lateral surface dose profiles could be obtained in addition to the surface dose at the centre of the field. The effects of bolus-skin gaps upon these lateral profiles will be discussed fully in Chapter 5.

In investigating the effects of bolus air gaps, the natural point of comparison is the surface dose absorbed when a bolus is present and in full-contact with the patient. Therefore, we proceed with our analysis by determining the surface dose as a function of gap size, relative to this reference condition, by defining the quantity $\Delta(g)$.

$$\Delta(g) = \frac{D_s(g)}{D_s(g=0)} \tag{4.1}$$

Where, D_s represents the dose at the phantom "surface", collected along the central beam axis. Of course, dose cannot practically be collected at the true surface (z=0). Therefore D_s, represents the dose at the shallowest possible measurement point for the given instrument. For MC phantoms this would be the centre of the first voxel (z = 0.0025 cm). This is the same effective depth of measurement as the Markus chamber. For EBT3 films, the depth of measurement is taken to be in the centre of the active layer at z=0.0189 cm. The quantity Δ can be described as representing the relative surface dose (in Gy), or a dimensionless Dose Reduction Factor (DRF).

As noted previously, parallel plate chambers are known to overestimate surface dose[25]. However, the deviation between the chamber measurements and the true surface dose is expected to be the equal for a given depth and a given chamber configuration, and is not influenced by the change in g. Therefore, any correction factor would be canceled out and we may determine Δ directly from the measurement of charge within the ionization chamber.

$$\Delta(g) = \frac{D_s(g)}{D_s(g=0)} = \frac{\overline{Q_s}(g)}{\overline{Q_s}(g=0)} \tag{4.2}$$

An average of four measurements, two values each for both positive and negative chamber voltages, was taken for the final value of charge. The relative errors of these charge values were less than 0.3%, resulting in relative errors of Δ of less than 0.1%.

For EBT3 measurements, surface dose values were obtained from FilmQA Pro dose maps in the same manner as the dose values used to create the PDD curves in Chapter 3. Similar precautions regarding film orientation, scan direction and the avoidance of possible edge effects were followed. Each film strip was marked at its centre so that it could be aligned with the central axis of the linac beam. Two 10 pixel by 10 pixel regions were selected above and below this mark. The average pixel value from both these regions was used to determine

$D_s(g)$ with typical standard errors of less than 0.03 cGy. The resulting errors in the ratio Δ were between 0.004 and 0.006.

A MATLAB script called "**getDsurf.m**" was used to extract surface doses from the MC and ECLIPSE^{TM} dose matrices and is described in the appendix.

4.3 Results and Discussion

In Figure 4.2, the results of our MC simulations are shown. The effects that bolus-skin gaps have on surface dose, as simulated in our models, are in general agreement with those observed by Khan and by other researchers [13, 44]. As described in Chapter 1, the introduction of an air gap reduces the surface dose as compared to the case where the bolus is in full-contact with the phantom. The relative dose is further reduced as the distance between the bolus and the phantom surface is increased. The scale of this decrease also depends on the field size, with larger fields demonstrating less loss in surface dose. Our MC results confirm these observations.

However, when compared to the results from Khan et.al our MC data shows greater dose reduction for similar gaps sizes using a given field. For example, for a 1 cm air gap and a 10 cm^2 field, MC determined DRF is $\Delta \approx 0.95$, whereas, Khan's measurement would suggest $\Delta \approx 0.99$. Similarly, Khan's findings indicate that the dose reduction is almost negligible for 15 cm^2 fields, even with a 5 cm gap. However, our simulations show a pronounced decrease in relative dose at all gap sizes.

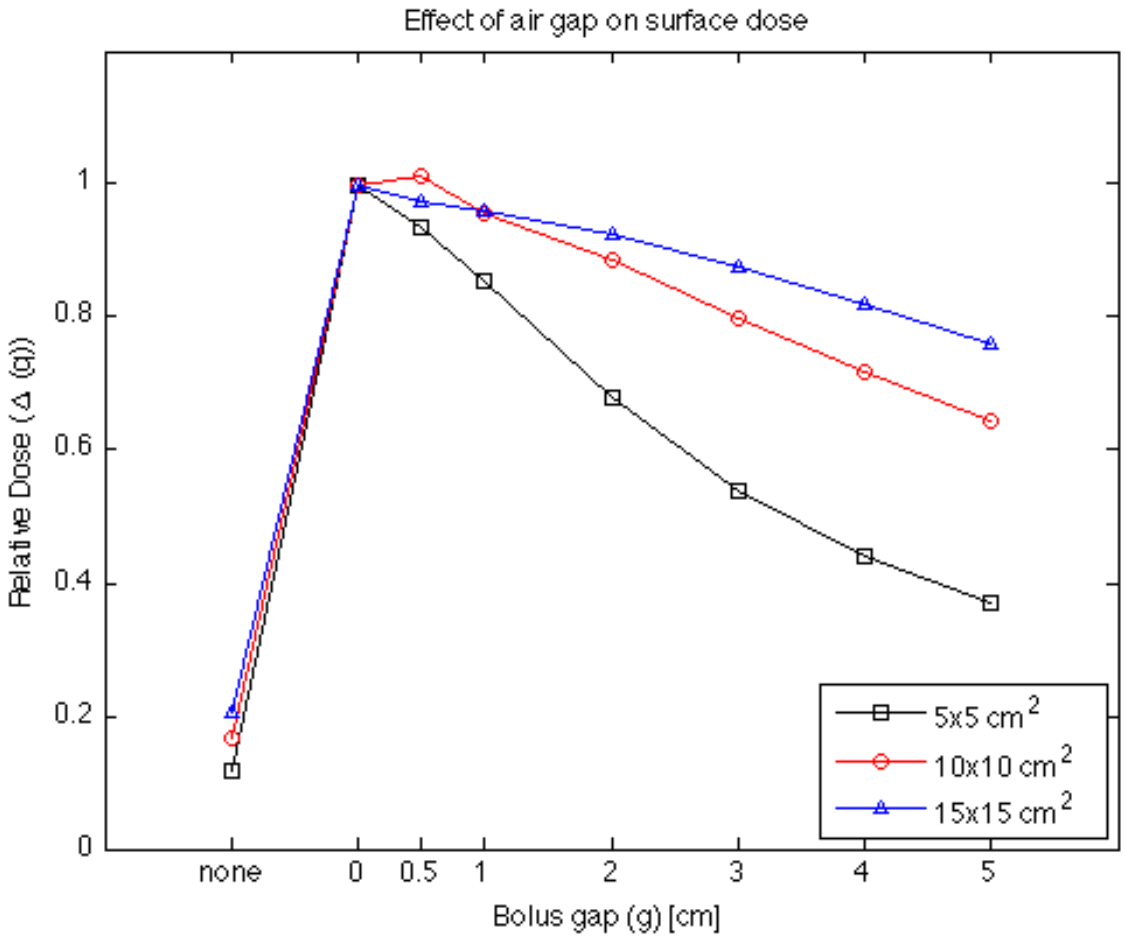

Figure 4.2: MC results showing effect of bolus-surface gaps (g) on surface dose. Doses are given normalised by the surface dose measured when no air gap is present ($g = 0$). Absolute errors in relative dose (Δ) are two small to be shown and were less than 0.006 for all field sizes. Bolus thickness was 1 cm.

Different sensitivities to the "gap-effect" are also apparent when comparing results obtained using different measurements methods. Figure 4.3 compares results from MC, AAA,EBT3 films and the Markus chamber from a 10x10 cm^2 field. It is clear that both the EBT3 films and the Markus chamber show different levels of surface dose reduction for comparable field sizes. The Markus results are particularly interesting as the chamber previously demonstrated

excellent agreement with MC calculations for PDD, but here shows substantially higher values for $\Delta(g)$.

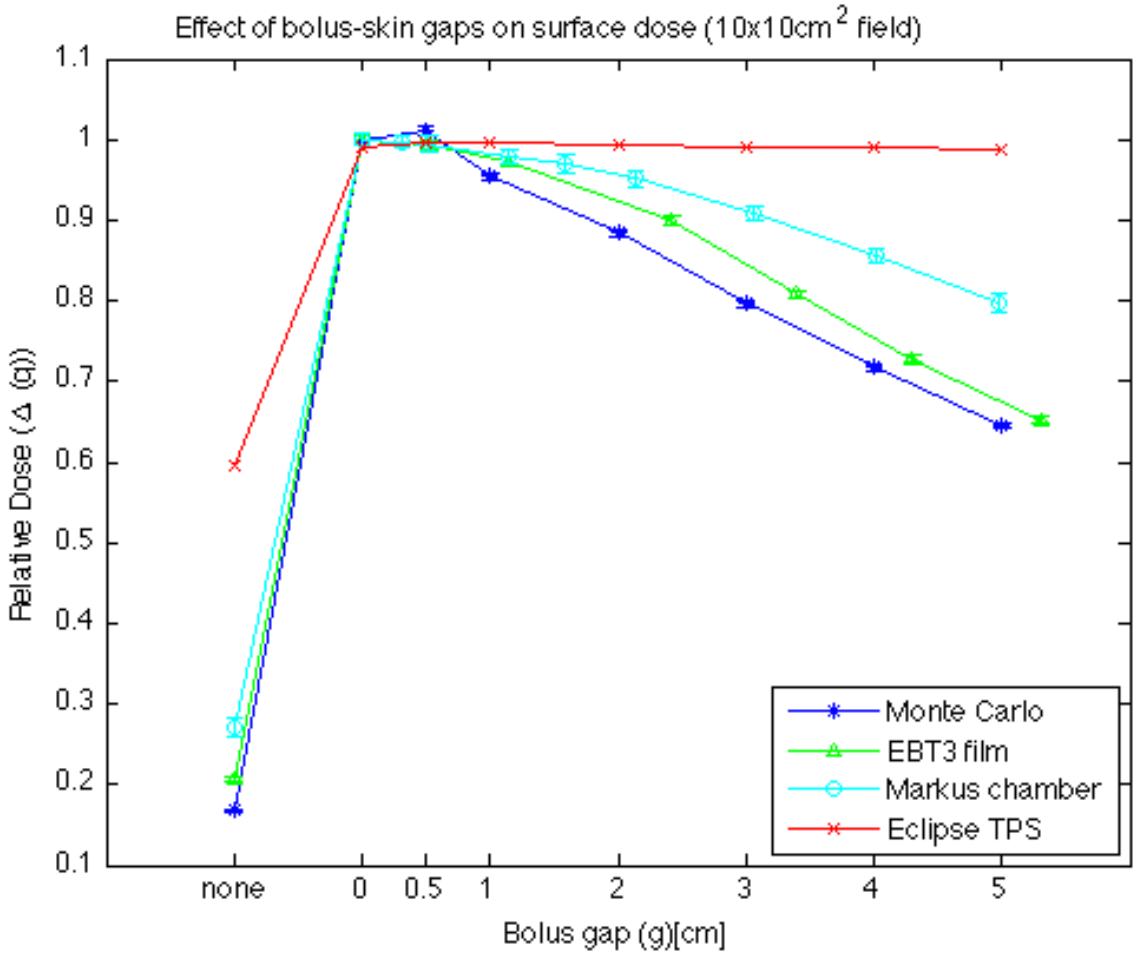

Figure 4.3: The effect of bolus-surface gaps on surface dose for a 10x10 cm^2 field as measured using MC, AAA, EBT3 films and a Markus parallel-plate ionization chamber. Bolus thickness = 1 cm

The varying sensitivities of the methods shown above can be elucidated by consideration of Figure 4.4. This Figure shows MC derived PDD curves in the first 1.5 cm of the phantom for gap sizes between 0 and 4 cm. It is apparent that large bolus-surface gaps result in the reestablishment of a dose build-up region, in agreement with the findings of Sroka et.al

[44]. The return of a high dose gradient in the near-surface region also brings back the issues with measuring doses in these gradients. Although the Markus chamber has a point of measurement comparable with that of MC, the chamber cavity is 2 mm thick, and so the dose is averaged over a large part of the new build-up region. The measured dose is still lower than the value obtained when $g = 0$, however, but less than one might measure if the charge could be collected over a smaller volume, therefore the Markus yields higher values of $\Delta(g)$. EBT3 has an active layer thickness of 28 μm, and so it has higher resolution than the Markus chamber. However, this active layer is at greater depth than the first voxel of the MC phantom and receives higher dose, therefore $\Delta(g)$ values obtained with EBT3 films are still higher than comparable values from MC.

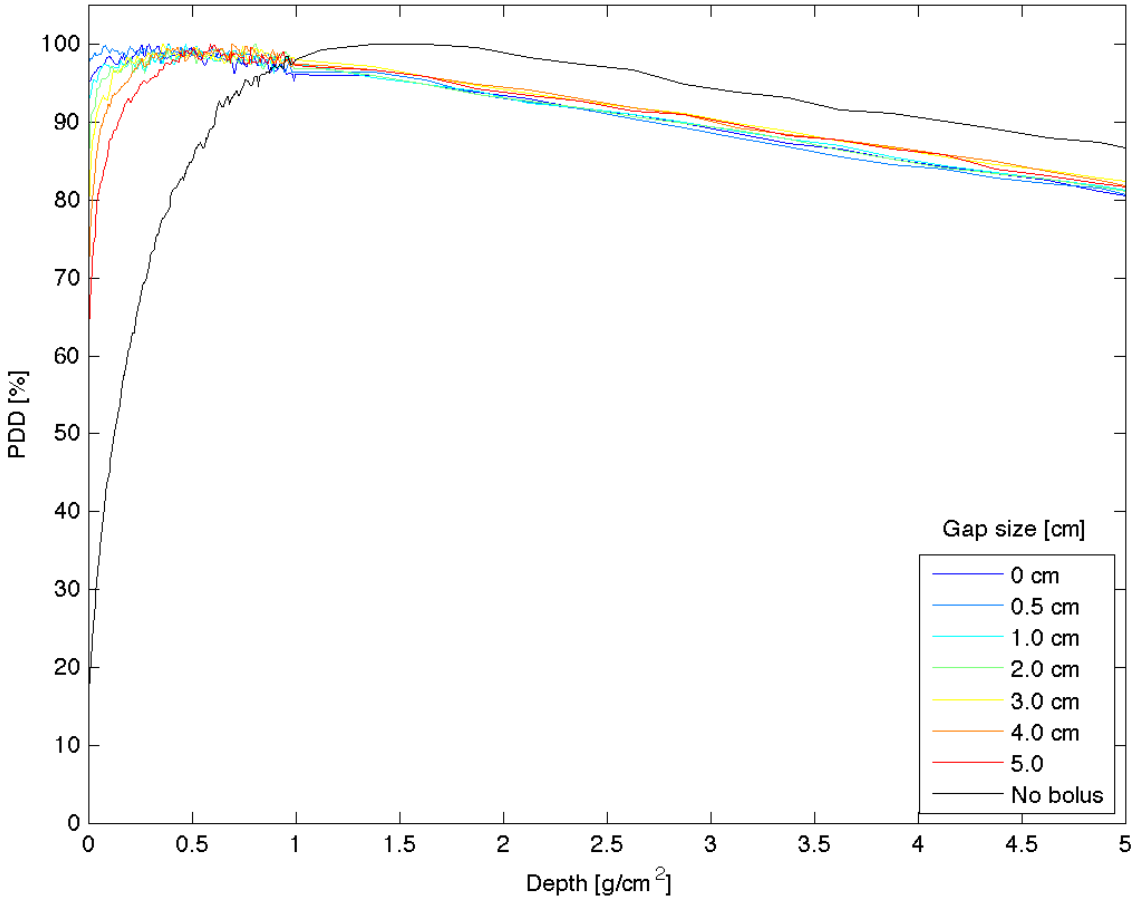

Figure 4.4: The effect of bolus-surface gap size on PDD (each curve is normalized to its own maximum dose), as shown for the first 5 cm. It can be seen that the presence of large gaps restores the build-up of dose near to the surface, in agreement with the results of Sroka et.al [44]. Bolus thickness = 1 cm

The reappearance of the build-up region confirms that the electronic equilibrium of the beam is significantly perturbed at large bolus-skin gaps. As discussed in Chapter 1, the dose at a given plane in the medium (transverse to the beam) is deposited by electrons that were set into motion at shallower depths. The application of bolus takes advantage of this effect by providing additional material to generate enough electrons to deposit higher doses in the patient's skin. However, with significantly lower density, air is a poor material for generating

electrons. Therefore, presence of an air gap between the bolus and the skin results in fewer electrons reaching the surface region and reduces the dose at the surface.

Sroka et.al suggested that at large gaps sizes, such that z_m is restored to its standard (without a bolus) value, the influence of the bolus can be ignored. However, we do not believe this to be entirely valid, as the electrons that are released from the bolus material will be present within the beam and will deliver dose to the surface. This will result in higher PDD in the near-surface region compared to values observed with no bolus present. Given the large CSDA range of electrons in air (0.1995 g/cm^2 [4] or $\approx$163 cm), this influence will persist for large gaps. The scale of this range would also suggest that very few of these bolus electrons will be lost from the beam. However, they are highly likely to be scattered and travelling through the air gap at angles relative to the central beam axis. The distribution of surface dose will, therefore, be spread over a wider area, which would have significant consequences for the accurate delivery of dose to a prescribed PTV. We will investigate this effect further in Chapter 5.

The most interesting result apparent from Figure 4.4, is that AAA calculations do not demonstrate any reduction of surface dose due to the presence of even large bolus-surface gaps. For all gap sizes between 0 and 5 cm, values of $\Delta(g)$ calculated in ECLIPSE^{TM} remain approximately constant. As AAA calculations were performed on virtual phantoms with 0.25 cm^3 voxels, it might be considered that the reduction of surface dose is simply averaged out in these larger voxels. However, the decrease in $\Delta(g)$ was observed in MC calculations performed at this voxel size. Therefore, we may conclude that the AAA algorithm does not account for changes in surface dose due to the presence of air gaps.

This result is not unprecedented as AAA calculations have been shown to be inadequate in describing dose calculations involving extreme heterogeneities. The 2015 work of E.A. Alhakeem found that AAA calculations failed to model any change in the PDD curves due to

the presence of an air cavity in the build-down region [7]. The results of this article and our own investigations seem to indicate that, although AAA can perform adequate calculations for anatomical inhomogeneities such as lungs [24, 42], it practically ignores extremely low density interfaces such as air cavities of bolus-surface gaps.

The AAA accounts for the presence of inhomogeneities by radiological scaling, i.e. the functions which describe the attenuation and scattering of photons and electrons are rescaled in each voxel i, and in all directions, by the relative electron density ρ_w [43, 46].

$$\rho_w = \frac{\rho_i^e}{\rho_{water}^e} \tag{4.3}$$

The relative electron density for air is ≈ 0.001, which would lead to very severe reductions to the energy-deposition functions and scattering kernels. One could speculate that in order to avoid the need for such dramatic corrections, the program includes a threshold density for applying the rescaling process. Media with densities as low as that of air could be assumed to have little practical effect on the distribution of dose, which is not unwarranted given how surface specific the dose reduction appears to be, and so the program does not attempt the rescaling. This could possibly explain why the AAA calculations do not appear to account for air gaps, either in our work or that of Alhakeem et.al, but does make some correction for lung inhomogeneities. Of course, the actual computer code that performs the AAA calculation is proprietary and so confirmation of this assumption would be difficult.

In conclusion, our results indicate that the presence of air gaps between a bolus and the patient's skin will reduce the central surface dose relative to that measured when the bolus is in full contact. The presence of an air gap has been shown to disrupt the electronic equilibrium of the beam and reestablish the build-up of dose in the near-surface region. These findings are in agreement with previous investigations on this subject. However, our investigations

also demonstrate that the AAA calculations do not appear to account for this effect, which could lead to inaccurate estimations of dose within patient treatment plans. Furthermore, our data shows that Monte Carlo simulations can model the effects of the bolus-surface gap and can be used to produce accurate dose calculations in clinical contexts, and to form the basis of a "virtual laboratory" in the exploration of this phenomenon.

Chapter 5

The Effects of Bolus-Skin Gaps on Lateral Dose Profiles

5.1 Introduction

The results of the preceding chapter demonstrate that the presence of an air gap between a bolus material and the patient can reduce the dose at the skin. It was also demonstrated that the AAA, a commercially available and widely-used dose calculation method, was unable to account for this effect. These findings have clear implications for treatment planning and delivery in clinical scenarios, especially if the treatment requires significant dose to the skin.

However, the magnitude of the dose is not the only parameter of key significance in treatment delivery. Radiotherapy methods, such as IMRT, sculpt and shape the three-dimensional distribution of dose with a high-degree of precision. For these techniques to operate successfully the shape and spread of dose within the medium must be well-characterised. Therefore, the potential effects that a bolus-skin gap has on dose-distribution must also be understood.

In this Chapter, we will analyse the effects of increasing air gap sizes upon the lateral surface dose profiles of a 6 MV treatment beam. Our analysis will concentrate on results obtained from the same MC simulations that yielded the results described in Chapter 4. We validate these findings using experimental data obtained from EBT3 film strips, which are well-suited to this task as they allow the measurement of dose across a 2D plane.

During the film experiments described in Chapter 4 (Figure 4.1b), long strips of EBT3 film were used so that line profiles along the X-axis of the beam could be also acquired. Profiles were obtained from the (FilmQA Pro) dose maps by isolating 10 pixel x 1000 pixel region of interest, centred upon the midpoint of each film strip. The dose values were then averaged along the short axis to create a single line profile.

It is important that any factors specifically affecting the shape and spread of the surface dose distribution are separated from the dose reduction effect observed in Chapter 4. To achieve this we have normalized each dose profile by its mean central dose. We refer to this relative dose value as $\Xi(x,g)$, which is a function of position on the x-axis and gap size (g) as follows:

$$\Xi(x,g) = \frac{D(x,g)}{D(x=0,g)} \tag{5.1}$$

For MC simulations, the value of $D(x=0,g)$ was determined as the average of the four central surface voxels. Experimental Ξ profiles were measured using the same central dose values that were used for the calculation of the relative dose Δ in the previous chapter.

5.2 Results and Discussion

Figure 5.1 compares MC calculated relative surface dose profiles, for a 10x10 cm^2 field and with air gaps in the range of 0- 5 cm, with those obtained experimentally using EBT3 film for a similar range of gap values. In both data sets we can clearly observe that the presence of an

air gap significantly alters the shape of the dose profile. When the bolus is in contact with the surface (g=0), the dose distribution closely matches the idealized "square" shape with little dose deposited outside the boundaries and approximately equal dose across the field's span. As the distance between the bolus and the phantom is increased the profiles becomes more "rounded". Dose near the inside edges of the field is reduced and there is a steady increase in dose outside of the field boundary for larger gap sizes.

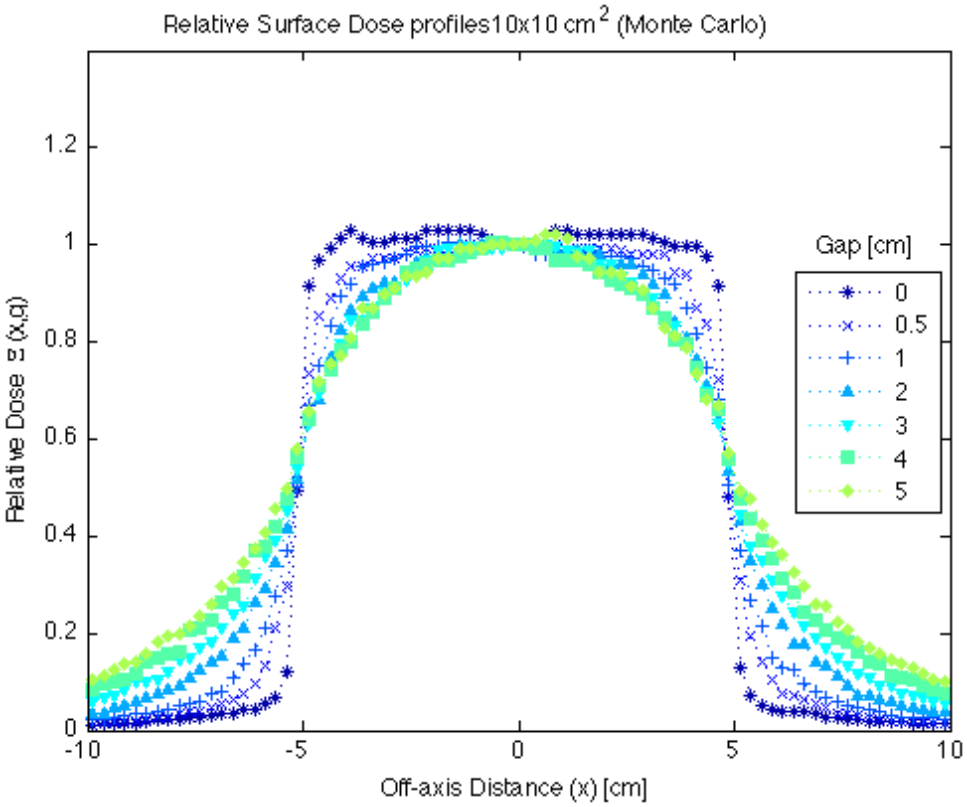

(a)

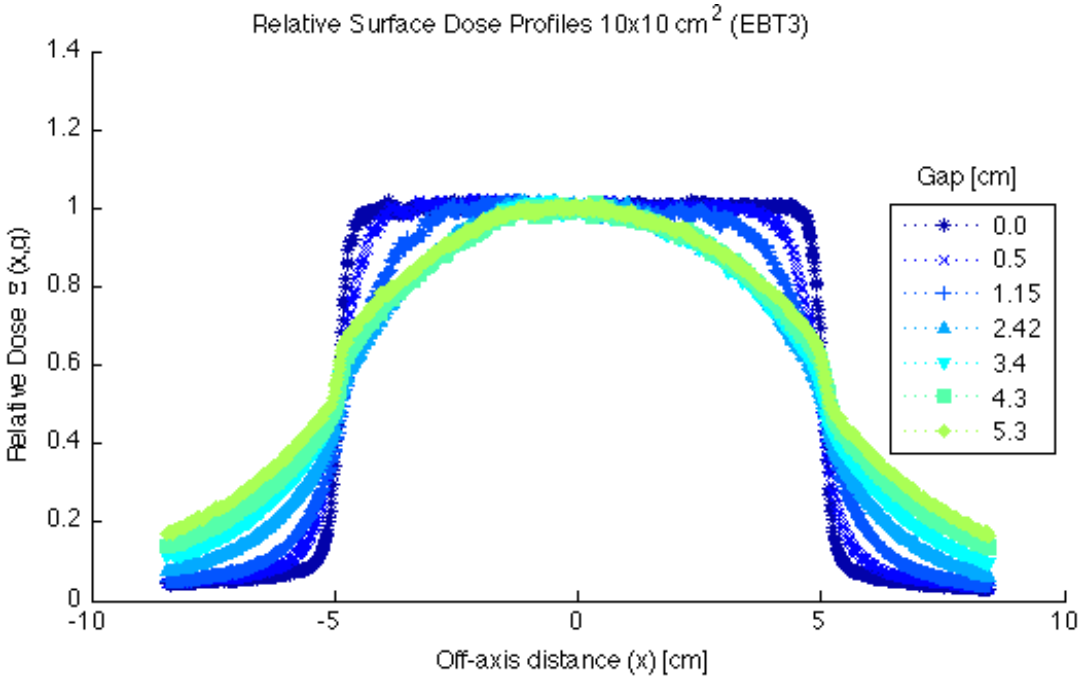

(b)

Figure 5.1: Variation in the shape of the lateral surface dose distribution due to increasing bolus-surface distance. Each profile presents the dose relative to the mean dose at the centre of the field ($\Xi(x,g)$). Data was derived from a) Monte Carlo and b) EBT3 film measurements. Bolus thickness = 1 cm.

The results from MC calculations show good agreement with the profiles obtained with film measurements. Both data sets clearly show the degradation of the beam profile as the gap-size increases. This is further support for the validity of our MC models as providing accurate reconstructions of the gap effect.

To quantify the spread of the beam profile we have measured the penumbra $p(g)$ as a function of the air gap size. The standard definition describes penumbra as the distance between the 80% and 20% isodose levels. Here we use a slightly modified definition and use the distance between the points of the profile where $\Xi(x,g)$ are equal to 0.8 and 0.2. However,

the MC results have a lateral resolution of 0.25 cm, which makes direct comparison with experimental values (resolution: 0.17 mm/pixel) more challenging.

Previous work in the literature has modelled the sigmoidal shape of the treatment beam edge using the *error function* [34]. However, we have found a related expression, the *Logistic function* provides a higher quality fit to our data. We have, therefore, used a non-linear least squares method to fit our relative dose profiles with the function described in Equation 5.2. This resulted in high-quality fits (R^2 values between 0.999-0.997) that were used to create approximate beam profiles from which more precise beam penumbra could be estimated.

$$\Xi(s) = \frac{A}{1 + e^{-k(s-s_0)}} + c \tag{5.2}$$

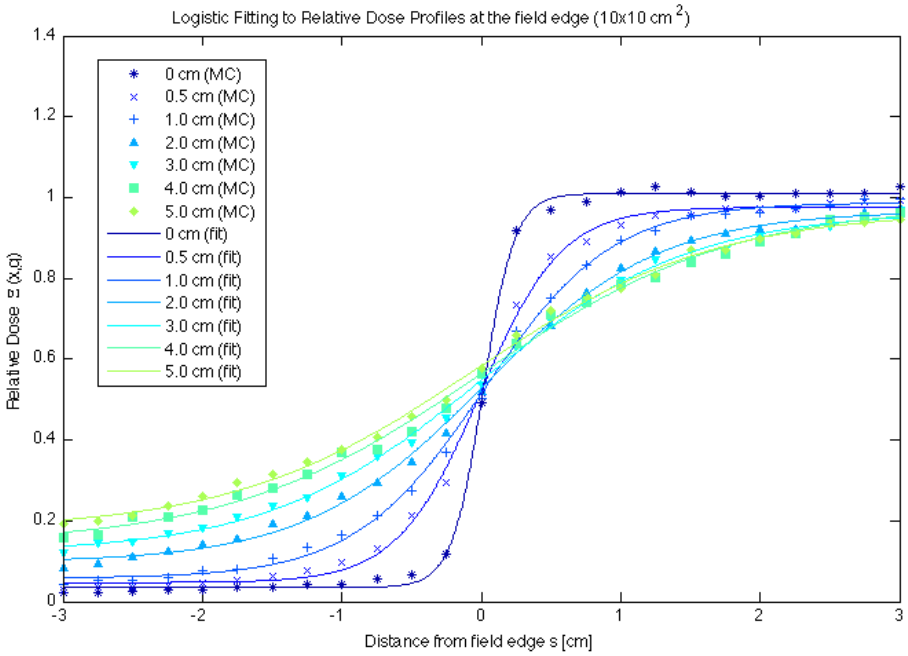

Figure 5.2: Monte Carlo calculated relative dose profiles for the edge of a 6 MV beam with 10x10 cm^2 field. The data points are fitted with the logistic function defined in Equation 5.2 (solid lines). Bolus thickness = 1 cm

The variable s represents the position along the beam's x axis, as measured from the field edge. The constants A, s_0 and k correspond to the curve's maximum value, midpoint and steepness, respectively. The dose profiles were sampled so that the data was centred upon the point where $\Xi(x,g) \approx 0.5$), which, based on standard definitions, is the approximate location of the beam edge as defined by the linac's light field. The quantity c can be interpreted as the minimum value of $\Xi(x,g)$ within the range of voxels studied. This value corresponds to the relative dose measured at the furthest point outside of the defined radiation field. The steepness parameter k provides a useful measure of the increasing spread of dose at larger gap sizes, with lower values indicating a higher degree of scatter.

The fitted coefficients for our MC data are shown below in Table 5.1. R^2 values are also provided as an indication of the quality of fit. Uncertainty was estimated by taking the RMS value of the 95% confidence bounds for each coefficient. The mean relative uncertainty in these fitted parameters was approximately 4%, 20%, and 10% for A,c and k, respectively. It can clearly be observed that, for all three field sizes, the steepness parameter decreases rapidly confirming the increased spread of dose at the phantom surface.

	5x5 cm^2					10x10 cm^2					15x15 cm^2				
g	A	c	k	s_0	R^2	A	c	k	s_0	R^2	A	c	k	s_0	R^2
0	0.987	0.019	9.536	0.017	0.999	0.975	0.035	8.918	0.012	0.999	0.960	0.047	9.348	0.032	0.999
0.5	0.967	0.031	3.548	0.006	0.999	0.929	0.047	3.409	-0.013	0.999	0.947	0.058	3.227	0.0042	0.999
1.0	0.954	0.046	2.478	-0.015	0.999	0.929	0.058	2.168	0.015	0.999	0.893	0.072	2.226	0.003	0.999
2.0	0.928	0.082	1.819	-0.061	0.999	0.870	0.097	1.578	0.013	0.998	0.844	0.104	1.505	-0.0017	0.998
3.0	0.892	0.121	1.661	- 0.112	0.998	0.845	0.121	1.314	-0.013	0.998	0.879	0.108	1.058	0.080	0.996
4.0	0.854	0.1661	1.630	-0.155	0.998	0.840	0.143	1.113	-0.004	0.997	0.764	0.149	1.139	-0.105	0.997
5.0	0.8133	0.202	1.661	-0.129	0.995	0.790	0.177	1.156	-0.048	0.998	0.766	0.172	1.036	0.037	0.996

Table 5.1: Coefficents obtained from fitting a Logistic function to the shape of lateral dose profiles.

The curves obtained from these logistic fits were then used to produce a more precise estimate of the dose penumbra in our MC results. Table 5.2 compares experimentally measured penumbra with those obtained from MC data using logistic curves.

MC fitted penumbra [cm]				Experimental penumbra [cm]			
g	5x5 cm^2	10x10 cm^2	15x15 cm^2	g	5x5 cm^2	10x10 cm^2	15x15 cm^2
0.0	0.29	0.32	0.32	0.0	0.33	0.34	0.32
0.5	0.82	0.93	0.94	0.5	0.75	0.83	N/A
1.0	1.21	1.44	1.51	1.2	1.27	1.52	1.52
2.0	1.75	2.24	2.53	2.4	1.96	2.64	2.89
3.0	2.12	2.86	3.35	3.4	N/A	3.18	N/A
4.0	2.54	3.51	3.98	4.3	2.79	3.82	N/A
5.0	3.50	4.00	4.44	5.3	3.05	4.22	N/A

Table 5.2: Values showing the dependence of profile penumbra on the size of bolus-surface air gaps. Experimental values were obtained directly from EBT 3 measurements. Values were estimated from MC results using logistic regression.

Both experimentally measured penumbra, and those determined from MC simulations, are shown to widen with increasing bolus-skin distance. The observed distortion of beam profiles has clear clinical implications, as dose is both reduced on the inside of the beam edge and increased outside of the boundary. In the context of a treatment plan this would result in an underdosing of the target with higher doses delivered to at-risk structures adjacent to the PTV.

However, the change in shape of the dose distribution was observed to be localised to the near-surface region as shown in Figure 5.3 for a 10x10 cm^2 field. Dose profiles taken at greater depths exhibit a "square" shape and are a closer match to the surface dose measured when the bolus is in direct contact with the phantom. Using Logistic regression, as described above, penumbra were determined from the MC dose matrices for increasing depth. Figure 5.3b shows the estimated penumbra, for each gap size, relative to the value found in the case of no air gap at the same depth. This penumbra decreases rapidly within the first millimetre of the phantom, and was found to reach unity within the first 7 mm of phantom depth. This was observed for all three field sizes studied and demonstrates that the effect of the scattered particles becomes negligible within a short distance of the phantom surface.

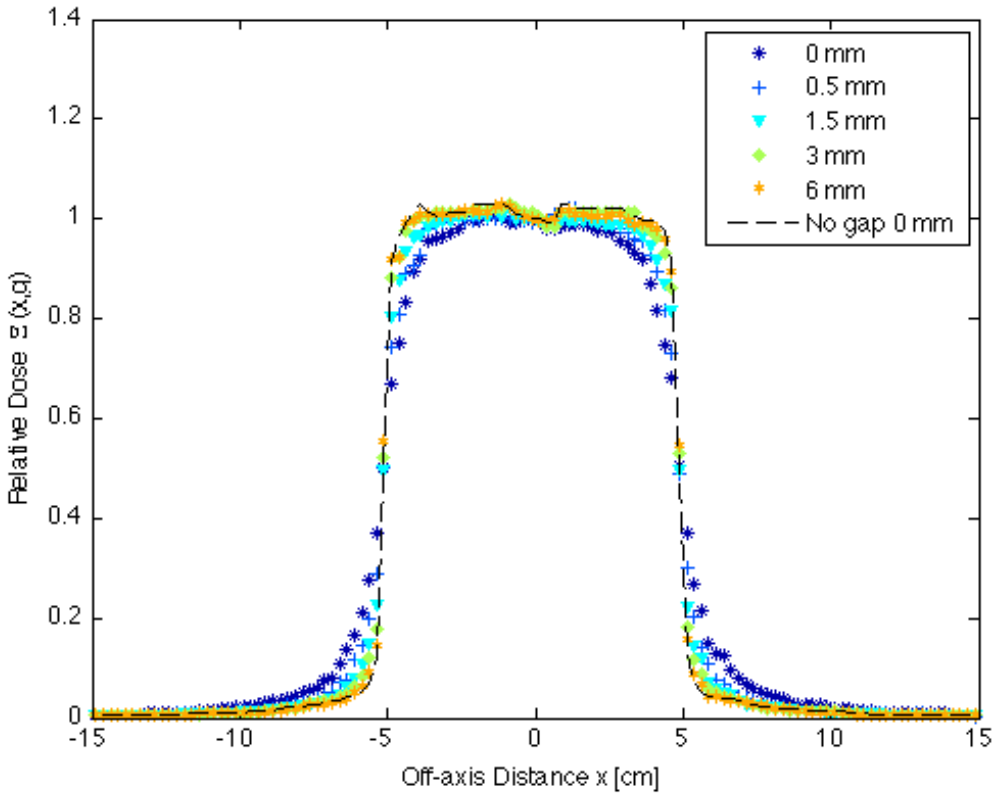
0 mm
0.5 mm
1.5 mm
3 mm
6 mm
No gap 0 mm
Relative Dose g (x,d)
Off-axis Distance x [cm]
1.4
1.2
1
0.8
0.6
0.4
0.2
0
-15
-10
-5
0
5
10
15

(a)

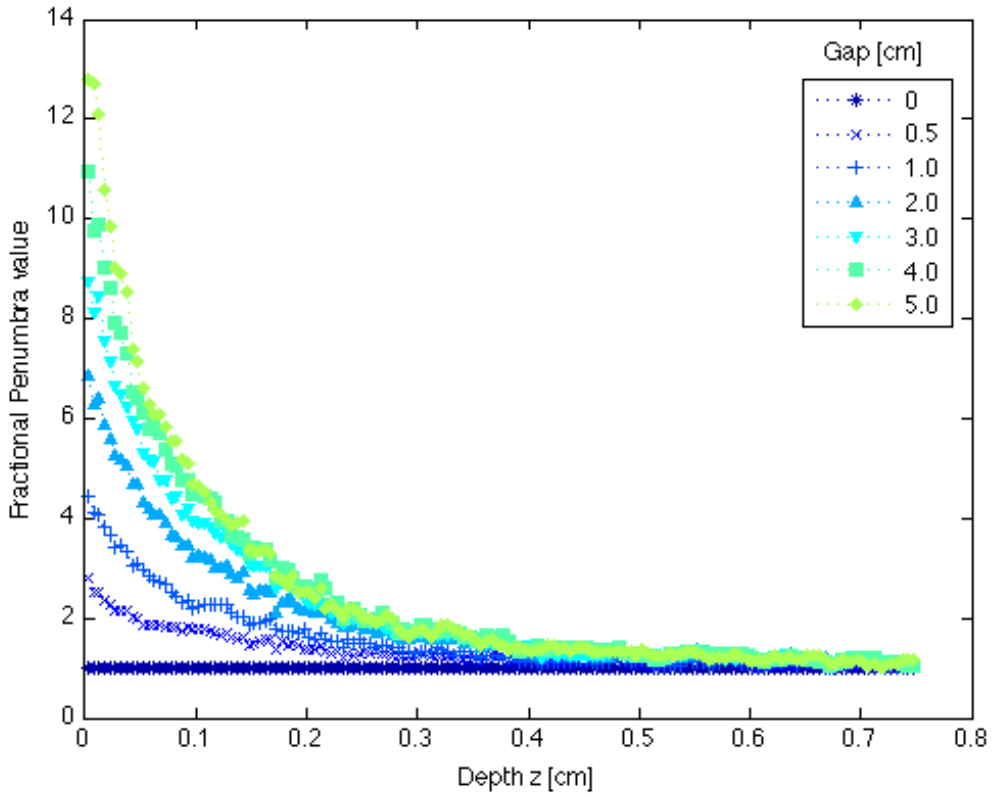

(b)

Figure 5.3: a) Lateral dose profiles for a 10x10 cm ^{2} at different depths. For comparison the black line represents the relative dose at the surface for g =0. b) Decrease of fractional penumbra (ratio of measured penumbra to corresponding value at $g = 0$) with depth. Bolus thickness = 1 cm

The correlation between increased gap size and the observed widening of the penumbra, and the surface specific nature of this effect, can be further understood by reference to the work of McKenna et.al regarding beam spoilers [34]. A beam spoiler is a layer of material, such as polystyrene, that is placed in the path of the beam in between the linac aperture and the patient. A "floating" bolus could therefore, be considered a beam spoiler. However, typical spoilers are placed at a much greater distance from the patient than would be expected from

a clinically relevant air gap between the bolus and skin. In both cases, a large fraction of the dose deposited at the surface layer of the material originates from electrons generated within the bolus/spoiler. McKenna and her colleagues used MC to create a simulated spectrum of these electrons, which was used to determine the energy deposition kernels of these electrons and, hence, their effect on dose. Their results also show a significant increase in the beam penumbra when applying a spoiler, as our results do in the case of a large bolus air gap.

When electrons are produced, via interaction with primary beam photons, in the bolus material they are incident upon the phantom surface with a narrow range of probable angles. The introduction of a gap between the bolus and the surface seems unlikely to significantly affect the probability distribution of these angles. However, increasing the distance between the phantom surface and the bolus will results in greater divergence for a given angle of incidence and, therefore, the electrons will be spread over a greater lateral distance. In this scenario, electrons emanating from a region near the beam edge will have a greater likelihood of passing out of the beam's defined field before reaching the surface. This will lead to a reduced number of electrons reaching the surface near the inside of the field boundary, and a greater number escaping to the outside edge. This produces the observed rounding of the dose profile at larger gap sizes. Another effect of greater beam divergence at large bolus-skin distances, would be to spread the incident electrons over a greater area. This would contribute to decreased surface dose on the central beam axis, as we have observed and was discussed in Chapter 4.

In conclusion, both MC simulations and radiochromic film experiments indicate that the distribution of surface dose would be substantially altered by the presence of an air gap, between the bolus and the patient's skin, during photon beam treatment. Our results show a pronounced decrease in dose near the inside boundary of the field, and a corresponding increase in dose outside of the field. This would suggest that the air gap effectively "spreads" out the

dose across the edges of the treatment field, which is likely due to increased scattering from secondary electrons originating within the bolus material. These findings have potentially important implications for clinical practise as this effect may lead to patient PTVs becoming underdosed whilst overdosing adjacent critical organs that should be spared. A main focus of future work would be to study this effect on more realistic treatment plans to determine if the magnitude of any resulting under/overdosing would be significant in a clinical context.

Chapter 6

Conclusions and Future Prospects

6.1 Conclusion

Bolus is a well-established method for adjusting the distribution of dose, during procedures using Megavoltage treatment beams, so that a greater amount of energy is deposited in the near-surface region. This technique has clear value for the treatment of tumours that are located closer to the skin, as are common in cancers of the head and neck. However, practical constraints such as the use of immobilization equipment and the natural contours of the human body can often prevent all parts of the bolus material being in complete contact with the skin. The resulting gaps would be expected to have a small but notable effect on the intensity of dose at the patient's skin. Given the rapid progress of radiotherapy, allowing the control of dose distribution to increasing precision, these small perturbations could become significant influences on patient treatment. Therefore, we have conducted this investigation to characterize the effects that bolus-skin gaps have upon surface dose distributions.

Our primary tool for our research has been MC simulations, and we have supported and validated the results of these calculations using ionization chamber and radiochromic film

measurements. Our findings indicate that the intensity of the surface dose, on the beams central axis, decreases as the distance between the surface and the bolus is increased. In addition, we have also shown that the distribution of dose at the surface is altered by the presence of an air gap. Regions near the interior edge of the treatment field received a reduced dose, whilst additional dose was measured outside of the defined treatment area. The results were consistent with a "spreading" of those dose likely caused by the additional scattering of electrons produced in the elevated bolus material.

During our investigation we have deliberately extended the size of the bolus-skin gap to investigate the relationship between surface dose and gap size. In clinical practise, the size of any notable gap between the bolus and the patient's skin would be highly unlikely to exceed 1 cm. At this scale, the reduction in relative surface dose is small, less than 10% for 5x5 cm^2 fields, and is likely to be smaller for realistic gaps sizes. The reduction in dose also appears to be limited to the near-surface region, and for the size of air gaps that might be conceivably encountered in clinical scenarios, the effect is negligible only a few millimetres from the surface. Therefore, in terms of dose to volume, the reduction in dose could be considered a minor effect.

However, rapid progress in modern radiotherapy techniques demand increasing accuracy and control over the magnitude and distribution of dose. In this sense our findings are relevant, particularly the observation of increased skin dose outside of the defined treatment field. In situations where the treatment plan has carefully sculpted the distribution of dose so as to avoid at-risk organs, the spread of dose beyond the planned beam edges is of clinical significance. Therefore, we suggest several ways that the research described in this thesis can be expanded upon.

6.2 Suggested Future Studies

For further investigations we would suggest addressing limitations of the current study and expanding upon it's findings. The research we have described in this thesis was intended to be the initial phase of work, aimed at demonstrating the extent of an effect of bolus-skin gaps on surface dose and identifying key areas for future study. As such, our simulations and research have considered only simple beam geometries and square field sizes. An initial extension of this investigation would be to study the influence of beam angles and beam shape on the bolus-gap effect. Suggested simulated experiments would include:

Influence of beam angles Several radiotherapy techniques, such as IMRT, make use of multiple treatment beams incident at different angles relative to the patient. Therefore, the effect of a bolus-surface gap at non-normal incidence is a clinically relevant question. MC simulations similar to those described in this thesis, could be performed over a wide range of angles of incidence. This investigation should include a treatment beam incident at 180°, i.e. a beam that would first pass through the phantom before irradiating the bolus slab. In the presence of a bolus-surface gap, such a treatment beam could generate electrons that are backscattered from the bolus to deposit dose on the patient's skin. The possibility of such an affect is worth investigation due to the common use of parallel opposing beams in radiotherapy.

Influence of non-square fields Our results demonstrate that the reduction in surface dose, caused by a bolus-surface gap, is increased for smaller field sizes. MC simulations of treatment beams using rectangular and circular fields should be conducted to determine if the scale of this effect is consistent using different field shapes. The influence of different field shapes on the observed scattering of dose in the near-field region would also be of interest.

Partially blocked beams As established in Chapter 5, the presence of an air gap between the applied bolus and the phantom surface significantly perturbs the distribution of dose in the field-edge region. The proposed cause of this effect was additional scattering of lower energy electrons that are generated within the bolus material. Therefore, it is possible that this effect could be exacerbated by the presence of additional contaminating electrons, such as those scattered from the beam collimators (in the case of a half-blocked beam) or the application of a beam wedge. Therefore, additional simulation should be conducted to elucidate these effects.

Dynamic Beam Shaping The results of our investigation indicate that the size of the treatment field, and additional scattering effects, influence the magnitude and distribution of surface dose in the presence of a bolus-surface air gap. However, techniques such as VMAT do not utilize static fields but, rather, use continuously moving mutli-leaf collimators to shape the dose during treatment. Therefore, the effects of bolus-air gaps should be investigated under the clinically relevant conditions of dynamic beam shaping. One question that should be addressed through MC simulations is: Does the reduction in surface dose, observed with small fields, persist if the beam profile is continuously adjusted, or is the effect "averaged out" during the treatment.

Clinical Treatment Plans In the 2013 study by Khan, the authors investigated the effects of bolus-surface gaps on surface dose deposited during IMRT treatment plans, which placed the work into more medically applicable context [30] . Similarly, further investigations with MC simulations should be used to establish the clinical relevance of the skin-dose reduction. In particular, the increase in dose measured outside of the treatment field should be investigated in treatment plans in which this additional scattering could potentially overdose nearby at-risk organs. One method for conducting such a study would be to introduce a bolus into virtual phantoms derived from patient

CT scans. However, a more direct approach would be to collect suitable examples of patient treatment plans where notable bolus air-gaps can be observed in the planning CTs. The size of the air gap could be established from the images in the ECLIPSE™ treatment plan.

The use of bolus in radiotherapy has a long history, stretching back to the beginning of the 20th century. However, despite the development of water-equivalent, synthetic media such as Superflab™, the general principle of shifting the point of dose maximum by applying a layer of additional material has not changed. Radiotherapy has undergone rapid progress in terms of accuracy and control over dose distribution, and the complexity of delivery methods. Therefore, reexamining time-tested techniques in context of modern methods is an important task. The work described in this thesis is intended to stimulate further study into the effects of bolus in modern radiotherapy, particularly addressing the presence of air gaps between the bolus and patient's skin. We have identified several lines of promising study to expand upon the results described in this investigation by further exploring the effects of bolus-surface gaps on surface dose, and placing the phenomenon in direct clinical context. We hope that our work stimulates further research into bolus and it's effects on the accurate control of dose distributions in radiotherapy.

Bibliography

[1] (2009). NIST attenuation coefficients. → pages 4

[2] (2015). Model n23343 Markus® Plane-Parallel ion chamber. → pages 51, 60, 62

[3] (2016). Gafchromic dosimetry media, type EBT-3. → pages 26, 61

[4] (2017). NIST ESTAR (Electron Stopping Power and Range Tables). → pages 81

[5] Abdel-Rahman, W., Seuntjens, J. P., Verhaegen, F., Deblois, F., and Podgorsak, E. B. (2005). Validation of Monte Carlo calculated surface doses for megavoltage photon beams. *Medical physics*, **32**(1), 286–298. → pages 40

[6] Akbas, U., Donmez Kesen, N., Koksal, C., and Bilge, H. (2016). Surface and buildup region dose measurements with Markus Parallel-Plate ionization chamber, GafChromic EBT3 film, and MOSFET detector for high-energy photon beams. *Advances in High Energy Physics*, **2016**. → pages 61

[7] Alhakeem, E. A., AlShaikh, S., Rosenfeld, A. B., and Zavgorodni, S. F. (2015). Comparative evaluation of modern dosimetry techniques near low-and high-density heterogeneities. *Journal of Applied Clinical Medical Physics*, **16**(5). → pages 34, 47, 82

[8] Almond, P. R., Biggs, P. J., Coursey, B., Hanson, W., Huq, M. S., Nath, R., and Rogers, D. (1999). AAPM's TG-51 protocol for clinical reference dosimetry of high-energy photon and electron beams. *Medical physics*, **26**(9), 1847–1870. → pages 20, 47

[9] Apipunyasopon, L., Srisatit, S., and Phaisangittisakul, N. (2012). An investigation of the depth dose in the build-up region, and surface dose for a 6-MV therapeutic photon beam: Monte Carlo simulation and measurements. *Journal of radiation research*, **54**(2), 374–382. → pages

[10] Behrens, C. (2006). Dose build-up behind air cavities for Co-60, 4, 6 and 8 MV measurements and Monte Carlo simulations. *Physics in Medicine Biology*, **51**(22), 5937. → pages

[11] Bergman, A. M. (2007). *Monte Carlo Simulation of Dose Distributions for Direct Aperture Optimization of Intensity Modulated Treatment Fields*. Ph.D. thesis, University of British Columbia. → pages

[12] Butson, M. J., Yu, P. K., Metcalfe, P. E., *et al.* (1999). Extrapolated surface dose measurements with radiochromic film. *Medical Physics*, **26**, 485–488. → pages

[13] Butson, M. J., Cheung, T., Yu, P., and Metcalfe, P. (2000). Effects on skin dose from unwanted air gaps under bolus in photon beam radiotherapy. *Radiation Measurements*, **32**(3), 201–204. → pages

[14] Butson, M. J., Cheung, T., Peter, K., and Currie, M. (2004). Surface dose extrapolation measurements with radiographic film. *Physics in medicine and biology*, **49**(13), N197. → pages

[15] Butson, M. J., Cheung, T., and Peter, K. (2006). Weak energy dependence of EBT gafchromic film dose response in the 50kVp–10MVp X-ray range. *Applied Radiation and Isotopes*, **64**(1), 60–62. → pages

[16] Cao, Y., Yang, X., Yang, Z., Qiu, X., Lv, Z., Lei, M., Liu, G., Zhang, Z., and Hu, Y. (2016). Superficial dose evaluation of four dose calculation algorithms. *Radiation Physics and Chemistry*. → pages

[17] Chakarova, R., Gustafsson, M., Bäck, A., Drugge, N., Palm, Å., Lindberg, A., and Berglund, M. (2012). Superficial dose distribution in breast for tangential radiation treatment, monte carlo evaluation of eclipse algorithms in case of phantom and patient geometries. *Radiotherapy and Oncology*, **102**(1), 102–107. → pages

[18] Chiu-Tsao, S.-T. and Chan, M. F. (2009). Photon beam dosimetry in the superficial buildup region using radiochromic EBT film stack. *Medical physics*, **36**(6), 2074–2083. → pages

[19] Cho, G. A., Ralston, A., Tin, M. M., Martin, D., Pickard, S., Kim, J., and Tse, R. (2014). In vivo and phantom measurements versus Eclipse TPS prediction of near surface dose for SBRT treatments. In *Journal of Physics: Conference Series*, volume 489, page 012008. IOP Publishing. → pages

[20] Chow, J. C., Jiang, R., and Leung, M. K. (2010). Dosimetry of oblique tangential photon beams calculated by superposition/convolution algorithms: a Monte Carlo evaluation. *Journal of Applied Clinical Medical Physics*, **12**(1). → pages

[21] Devic, S., Seuntjens, J., Abdel-Rahman, W., Evans, M., Olivares, M., Podgorsak, E., Vuong, T., and Soares, C. G. (2006). Accurate skin dose measurements using radiochromic film in clinical applications. *Medical physics*, **33**(4), 1116–1124. → pages

[22] Devic, S., Aldelaijan, S., Mohammed, H., Tomic, N., Liang, L.-H., DeBlois, F., and Seuntjens, J. (2010). Absorption spectra time evolution of EBT2 model Gafchromic film. *Medical physics*, **37**(5), 2207–2214. → pages

[23] Devic, S., Tomic, N., and Lewis, D. (2016). Reference radiochromic film dosimetry: review of technical aspects. *Physica Medica*, **32**(4), 541–556. → pages

[24] Gagne, I. M. and Zavgorodni, S. (2007). Evaluation of the analytical anisotropic algorithm (AAA) in an extreme water-lung interface phantom using Monte Carlo dose calculations. *Journal of Applied Clinical Medical Physics*, **8**(1). → pages

[25] Gerbi, B. J. and Khan, F. M. (1990). Measurement of dose in the buildup region using fixed-separation plane-parallel ionization chambers. *Medical physics*, **17**(1), 17–26. → pages

[26] Johns, H. E. and Cunningham, J. R. (1974). *Physics of Radiology*. Charles River Media. → pages

[27] Kawrakow, I. (2002). On the de-noising of Monte Carlo calculated dose distributions. *Physics in Medicine Biology*, **47**(17), 3087. → pages

[28] Kawrakow, I. (2006). On the effective point of measurement in Megavoltage photon beams. *Medical physics*, **33**(6), 1829–1839. → pages

[29] Khan, F. M. and Gibbons, J. P. (2014). *The physics of radiation therapy*. Lippincott Williams & Wilkins. → pages

[30] Khan, Y., Villarreal-Barajas, J. E., Udowicz, M., Sinha, R., Muhammad, W., Abbasi, A. N., and Hussain, A. (2013). Clinical and dosimetric implications of air gaps between bolus and skin surface during radiation therapy. *Journal of Cancer Therapy*, **4**(7), 1251. → pages

[31] Kim, J.-H., Hill, R., and Kuncic, Z. (2012). An evaluation of calculation parameters in the EGSnrc/BEAMnrc Monte Carlo codes and their effect on surface dose calculation. *Physics in medicine and biology*, **57**(14), N267. → pages

[32] Lee, N., Chuang, C., Quivey, J. M., Phillips, T. L., Akazawa, P., Verhey, L. J., and Xia, P. (2002). Skin toxicity due to intensity-modulated radiotherapy for head-and-neck carcinoma. *International Journal of Radiation Oncology* Biology* Physics*, **53**(3), 630–637. → pages

[33] McEwen, M., Kawrakow, I., and Ross, C. (2008). The effective point of measurement of ionization chambers and the build-up anomaly in MV X-ray beams. *Medical physics*, **35**(3), 950–958. → pages

[34] McKenna, M. G., Chen, X. G., Altschuler, M. D., and Bloch, P. (1995). Calculation of the dose in the build-up region for high energy photon beam: Treatment planning when beam spoilers are employed. *Radiotherapy and Oncology*, **34**(1), 63–68. → pages

[35] Nilsson, B. and Montelius, A. (1986). Fluence perturbation in photon beams under nonequilibrium conditions. *Medical physics*, **13**(2), 191–195. → pages

[36] Panettieri, V., Barsoum, P., Westermark, M., Brualla, L., and Lax, I. (2009). AAA and PBC calculation accuracy in the surface build-up region in tangential beam treatments. phantom and breast case study with the Monte Carlo code PENELOPE. *Radiotherapy and Oncology*, **93**(1), 94–101. → pages

[37] Parsai, E. I., Shvydka, D., Pearson, D., Gopalakrishnan, M., and Feldmeier, J. J. (2008). Surface and build-up region dose analysis for clinical radiotherapy photon beams. *Applied Radiation and Isotopes*, **66**(10), 1438–1442. → pages

[38] Popescu, I., Shaw, C., Zavgorodni, S., and Beckham, W. (2005). Absolute dose calculations for Monte Carlo simulations of radiotherapy beams. *Physics in medicine and biology*, **50**(14), 3375. → pages

[39] Recommendations, I. (1990). ICRP publication 60. *Annals of ICPR*, **21**(1-3). → pages

[40] Rink, A., Vitkin, I. A., and Jaffray, D. A. (2007). Energy dependence (75kVp to 18MV) of radiochromic films assessed using a real-time optical dosimeter. *Medical physics*, **34**(2), 458–463. → pages

[41] Robinson, D. (2008). Inhomogeneity correction and the analytic anisotropic algorithm. *Journal of Applied Clinical Medical Physics*, **9**(2), 112–122. → pages

[42] Rønde, H. S. and Hoffmann, L. (2009). Validation of varian's AAA algorithm with focus on lung treatments. *Acta Oncologica*, **48**(2), 209–215. → pages

[43] Sievinen, J., Ulmer, W., Kaissl, W., *et al.* (2005). AAA photon dose calculation model in eclipse. *Palo Alto (CA): Varian Medical Systems*, **118**, 2894. → pages

[44] Sroka, M., Reguła, J., and Łobodziec, W. (2010). The influence of the bolus-surface distance on the dose distribution in the build-up region. *Reports of Practical Oncology & Radiotherapy*, **15**(6), 161–164. → pages

[45] Takeuchi, A., Raich, T., Yoshida, R., Kojima, K., Niwa, M., Komori, M., and Oguchi, H. (2013). Effect of the difference in electron cutoff energy on surface dose calculation in the Monte Carlo linear accelerator simulation of megavoltage photon beams. In *Proceeding of the 20th EGS Users Meeting in Japan, KEK Proc*, volume 6, page 30. → pages

[46] Van Esch, A., Tillikainen, L., Pyykkonen, J., Tenhunen, M., Helminen, H., Siljamäki, S., Alakuijala, J., Paiusco, M., Iori, M., and Huyskens, D. P. (2006). Testing of the Analytical Anisotropic Algorithm for photon dose calculation. *Medical physics*, **33**(11), 4130–4148. → pages

[47] Velkley, D., Manson, D., Purdy, J., and Oliver Jr, G. (1975). Build-up region of Megavoltage photon radiation sources. *Medical physics*, **2**(1), 14–19. → pages

[48] Vyas, V., Palmer, L., Mudge, R., Jiang, R., Fleck, A., Schaly, B., Osei, E., and Charland, P. (2013). On bolus for Megavoltage photon and electron radiation therapy. *Medical Dosimetry*, **38**(3), 268–273. → pages

[49] Walters, B., Kawrakow, I., Rogers, D., *et al.* (2005). DOSXYZnrc users manual. *NRC Report PIRS 794*, **206**. → pages

[50] Walters, J., Ryan, S., and Harmon, J. F. (2012). Characterization of differences in calculated and actual measured skin doses to canine limbs during stereotactic radiosurgery using gafchromic film. *Medical Dosimetry*, **37**(2), 201–207. → pages

Appendix A

Supporting Materials

In this appendix we provide the code for the key scripts used in the analysis of the **.3ddose** files that were output from our Monte Carlo (MC) simulations. This is not an exhaustive list of all analysis performed in our investigation. However, most further processes utilize and build upon these core functions.

A.1 getPDD.m

This script was utilized to extract, store and plot the calculated Percentage Depth Dose (PDD) profiles.

The inputs to the script are:

- The .3ddose files containing the calculated relative dose, and associated errors, in each voxel. This can be entered in the function call or by GUI.
- The coordinates to define where on the surface the profiles is measured. The default is to measure the PDD along the central beam axis.

The outputs are:

- The PDD profile and the associated absolute errors.
- The maximum dose measured along the profile and it's error.

```
function [PDD,errPDD,Dmax,err_Dmax] =
    getPDD(DoseFileName,error,point);

%GETPDD - Calculates/plots Percentage Depth Dose from a given
    3ddose file.

%DoseFileName = input('Insert filename string')

% If a dose matrix (present in workspace) is specified load dose
    from GUI
% or filename string.
if or(isempty(DoseFileName),ischar(DoseFileName))
[dose,error,bounds] = read3ddose_Abs(DoseFileName);
else
   dose = DoseFileName; % Proceed if fed matrices in workspace.
end

nvox = size(dose) % Number of voxels
spc = 30.0/nvox(1); %Spacing of voxels
spc = round(spc*100)/100

% Depth here refers to the depth of the air block above the phantom
% surface i.e. the location of the phantom surface.

%Find the voxel index of phantom surface.
```

```
if nvox(3) == 2*nvox(1) % This applies to phantoms with uniform
    0.25 cm3 voxels.
   depth = 30;
   depth_idx = round(depth/spc)
   z = bounds{3}
elseif nvox(3) > 2*nvox(1) % This applies to those phantoms with
    high-resolution
   depth = 30;       % voxels in the near surface region.
   %depth_idx = 41
   depth_idx = find([diff(bounds{3})<0.1],1)-1
   z = bounds{3};
else
   depth_idx = nvox(3)-nvox(1); % This would apply to Eclipse dose
      matrices.
   depth = depth_idx*spc
   z = [0:spc:(nvox(3)-1)*spc];
end

% This if statement allowed for PDD curves to be taken off of the
    central
% axis at a position defined by the input "point"
if isempty(point)
   prof_loc = nvox./2; % Find the centre of the phantom.
else
   prof_loc = (point+15.0)./spc;
end
```

```
XDP = dose(prof_loc(1):prof_loc(1)+1,prof_loc(2):prof_loc(2)+1,:);
    % Take 4x4 cross-sectional profile through phantom
DDP = squeeze(mean(mean(XDP,1),2)); % Average into single profile.
DDP = medfilt1(DDP);
[Dmax,idx] = max(DDP(depth_idx+1:nvox(3))) % Find maximum dose &
    depth-index of voxel

dmax = z(depth_idx+idx)% Determine depth of maximum dose
disp('Double-check this with data-browser!!!')

%Convert to percentage depth dose
PDD = (DDP./Dmax);
PDD = PDD*100;

if ~(isempty(error))
    XEP = error(prof_loc(1):prof_loc(1)+1,
        prof_loc(2):prof_loc(2)+1,:);
    XEP = (XEP.*XDP).^2;
    XEP = squeeze((sqrt(sum(sum(XEP,1),2)))/4); % Error in averaged
        profile
    XEP = (XEP./DDP); %Relative error
    err_Dmax = XEP(idx); % Error in Dmax
    errPDD = (sqrt((XEP.^2) + err_Dmax^2));%Relative error in PDD;
    errPDD = (errPDD.*PDD); %Absolute error in PDD
    figure()
    errorbar(z(depth_idx+1:end),PDD(depth_idx+1:end),errPDD(depth_idx+1:end))
    errPDD = errPDD(depth_idx+1:end);
else
```

```
    figure()
    plot(z(depth_idx+1:end),PDD(depth_idx+1:end))
    %plot(z((nvox(3)/2)-2:end),PDD((nvox(3)/2)-2:end))
end

PDD = PDD(depth_idx+1:end);

title('Central Percentage Depth dose profile')
xlabel('Z (cm)')
ylabel ('Relative Dose (%)')
```

A.2 getDsurf.m

This script is a compliment to getPDD and determines the calculate surface dose along the central beam axis from a .3ddose file.

The inputs include:

- The 3ddose files containing MC doses and/or it's errors, which can be chosen using a GUI.

The outputs are:

- The magnitude of dose, along the central beam axis, at the surface of the phantom, and it's estimated error.

```
function [Dsurf, DSerr] = getDsurf(DoseFileName,error);

%Alows you to run with either a preloaded dose matrix, a typed in
    dose file
```

```
%name or a GUI browser.

if or(isempty(DoseFileName),ischar(DoseFileName))
[dose,error,bounds] = read3ddose_Abs(DoseFileName);
else
   dose = DoseFileName; % Proceed if fed matrices in workspace.
end

nvox = size(dose)

% These lines allow for different phantom types to be accounted for

if nvox(3) >= 2*nvox(1)
   depth = 30;
   %depth_idx = 41
   depth_idx = find([diff(bounds{3})<0.1],1)-1
   z = bounds{3};
else
   depth_idx = nvox(3)-nvox(1);
   %spc =
   %depth = depth_idx*spc
   %z = [0:spc:(nvox(3)-1)*spc];
end

%Find the voxel index of phantom surface.
mid = nvox(1)/2;

%Get dose and error from 4 central surface voxels.
```

```
Dsurf = dose(mid-1:mid+2,mid-1:mid+2, depth_idx+1);

if ~(isempty(error))
   DSerr = error(mid-1:mid+2,mid-1:mid+2, depth_idx+1);
   DSerr = DSerr.*Dsurf; % Convert to absolute voxel error.
   %Get absolute error in Surface Dose (using quadrature formula)
   DSerr = sqrt(sum(DSerr(:).^2))/16
end

Dsurf = mean(mean(Dsurf,1),2) % Mean Surface dose
```

A.3 Yprofs.m

This code was used to measure and plot lateral dose profiles from the results of MC calculations. The scripts determines and plots lateral dose profiles at depths of 0.5 cm, 1.5 cm, 3.0 cm, and 6 cm, from the phantom surface.

The inputs to the function are:

- A string containing the name of a 3ddose file, or one can be selected from a GUI interface.

The outputs are:

- A matrix containing lateral dose profiles at each of the specified depths.

```
[dose,error,bounds] = read3ddose_Abs(DoseFileName);
else
   dose = DoseFileName; % Proceed if fed matrices in workspace.
end
```

```
nvox = size(dose);
spc = 30.0/nvox(1);
spc = round(spc*100)/100 ;
mid = nvox(2)/2;

if nvox(3) >= 2*nvox(1)
   depth = 30;
   %depth_idx = 41
   depth_idx = find([diff(bounds{3})<0.1],1);
   prof_d = [0, 10 ,30, 60 ,120] + depth_idx;
   y = bounds{2};
else
   depth_idx = nvox(3)-nvox(1)+1;
   prof_d = [0, 3, 4, 200] + depth_idx;
   depth = depth_idx*spc
   y = [-15.0:spc:14.75]+spc/2;
end

l = dose(mid:mid+1,:,prof_d);
line_av = mean(squeeze(l),1) ;
Y_sects = squeeze(line_av);
centre_av = mean(Y_sects(mid-1:mid+2,:),1);
Y_sects = bsxfun(@rdivide,Y_sects,centre_av);
Y_sects = medfilt1(Y_sects);
end
```